ABSTRACT

Title of Thesis: MONOLITHIC IN-PLANE TUNABLE OPTICAL

FILTER

Degree Candidate: Jonathan Adam McGee

Degree and Year: Masters of Science, 2008

Thesis Directed By: Dr. Reza Ghodssi, Electrical and Computer

Engineering

This thesis presents the development of a Micro-Electro-Mechanical System (MEMS) monolithic in-plane tunable optical filter in both Indium Phosphide and Silicon. By placing one mirror of a waveguide-based Fabry-Perot interferometer on an electrostatically-actuated beam, a tunable filter is constructed. This is the first demonstration of a waveguide-coupled MEMS tunable optical filter in any material system. Filters with a tuning range of 40 nm from a wavelength 1550 nm with a linewidth of 35 nm are demonstrated. Future work will concentrate on improving the filter's optical characteristics, limited by etch-induced facet roughness, and integration with active photonic devices.

MONOLITHIC IN-PLANE TUNABLE OPTICAL FILTER

By

Jonathan Adam McGee

Thesis submitted to the Faculty of the Graduate School of the
University of Maryland, College Park, in partial fulfillment
of the requirements for the degree of
Master of Science
2008

Advisory Committee:
Professor Reza Ghodssi, Chair
Professor Christopher Davis
Professor Agis Iliadis

Acknowledgments

We start our graduate studies helpless as a newborn babe. In that vein, it is important for me to thank those who raised me and contributed to my success.

I would first like to thank the R22 group and cleanroom staff of LPS, especially Steve Brown, Dan Hinkel, Lisa Lucas, and Toby Olver, for their assistance in fabrication backed by countless hours of training and companionship during long hours of processing.

A hail to the MBE research group at LPS, S. Kanakaraju and Chris Richardson, for providing the Indium Phosphide growths used in this research.

Peace to the members of the MEMS Sensors and Actuators Lab for their continual assistance, discussions, and support. Greatest amongst them, Stephan Koev for keeping me honest when it comes to math, Nathan Siwak for spending long nights next to the warm glow of the RIE, and Michael Khbeis for the much of the machinery used in the study of silicon.

Finally, I would like the defense committee, Professor Chris Davis, Professor Agis Iliadis, and especially Professor Reza Ghodssi, for his continued guidance and support through this degree process.

Contents

Chapter 1

Introduction

In every modern photonic and optical device, significance is attached to the wavelength of light. It can be as basic as the range where optics are transparent or optical sources are active. However, in many applications, wavelength can act as a source of information itself. A device, such as a tunable filter, which can extract this information has considerable utility.

1.1 Motivation

1.1.1 Telecommunications

In telecommunications systems, the cost of individual fibers is quite high. This expense stems not from the physical cost of the fiber, but from the cost of installation. In order to maximize the value of this installation while bandwidth steadily increases, data carriers replace a single optical

source with several of different wavelengths. Each wavelength carries different information (known as Wavelength Division Multiplexing), linearly increasing a fiber's capability with increasing sources.

However, it is necessary to separate these wavelengths for the data to be recovered. If the full multiplexed signal is delivered to a detector, only a garbled mix of the constituent data will be received. It is, therefore, necessary for a filter to be installed prior to the receiver. For the major optical backbones, this task is performed by small numbers of statically-tuned add/drop multiplexers.

While deployment of high-speed fiber communications to the home is possible, as illustrated by Verizon's FiOS service, it remains an expensive endeavor. It is important to minimize the amount of fiber laid, but still provide a full data stream per user. Currently, this need is served through Time-Division Multiplexing (TDM); however, TDM makes only a small fraction of the available bandwidth of the fiber available. In order to provide future room for consumer's insatiable appetite for bandwidth, it is necessary to eventually turn to WDM to increase the bandwidth utilization of installed fiber.

However, unlike the large metropolitan networks, these networks need to reconfigure frequently. As users join and leave the network and new regions are brought on-line or upgraded to handle increased load, it may be difficult to maintain simple wavelength assignments for each user. Further, given the enormous number of installations in a consumer network,

attempting to use statically-tuned multiplexers would be a inventory and service nightmare. What is necessary is a method for the end-user's installation to tune the source and receiver to match the transitory requirements of the network without needing to replace filters or other components.

These requirements have been a major impetus for the development of low-cost microfabricated tunable filters.

1.1.2 Spectroscopy

As interest in the telecommunications market dies down, research interests by optical experts has turned to biological systems. Complex molecules, such as those in biology, interact with light in sophisticated ways, making it possible to measure their interactions quantitatively and make qualitative decisions as to the identity of chemicals.

One of the major avenues of research has been the miniaturization of spectrometers. This is based on the principle that molecules and atoms, being quantum systems, have their vibrations and potential energy quantized. The unit of quantization is a function of the atoms, bond lengths, strengths, and electron distributions. The combination of all these resonances is unique for a given molecule. This quantization can be inferred from optical measurement. Photons possessing energies exceeding this quantization will be more readily absorbed and photons equal to the quantization may be released in response to excitation. Additionally, some fraction of incident light may be shifted in energy by the quantization energy.

3

If it is possible to scan the optical response of a substance as a function of wavelength, it is possible to determine the constituent components of the substance. Traditionally, spectrometers are large optoelectronic devices; however, operating under a simple principle: filtering light through a monochromator prior to measurement by an optical power meter. The development of miniaturized narrow-band tunable filters could fulfill the role of the monochromator, allowing these large, complex machines to be made small and cheap while still providing the full diagnostic capabilities. Such devices could find their way into doctor's offices and homes, quickly performing in minutes the complex chemical analyzes that have conventionally required large laboratories and days.

1.2 Literature Review

The development of tunable optical filters is extensive, spread over a wide variety of techniques and materials. However, in the interest of relevance, the review will be limited to those devices exploiting the same basic technique as that described in this thesis: the use of a tunable resonant cavity. A one-dimensional resonant cavity composed of two reflective surfaces is known as a Fabry-Pérot interferometer or etalon. By changing the optical path length between the mirrors, the resonant modes of the cavity are shifted. The most significant difference in approach between the filters discussed is how the optical path length is modulated. Each technique

4
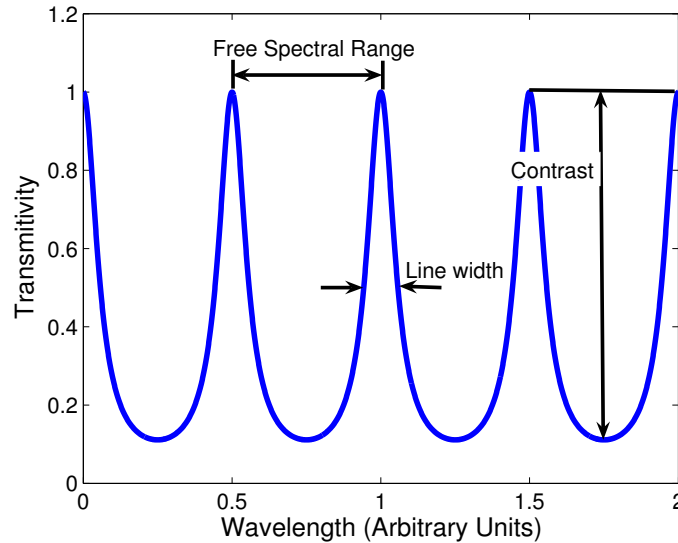
Figure 1.1: Illustration of major filter characteristics.

will be introduced individually and then contrasted in the final section.

1.2.1 Basic Concepts

When discussing filters, several optical characteristics are frequently used and need to first be defined. These characteristics are illustrated in figure 1.1 and defined below.

Linewidth describes the spectral width of the filter's passband. If the passband approximates a peak, it is frequently defined as the Full-Width Half-Max (FWHM). In the literature, it is common to see it expressed in both free space wavelength and frequency as these two concepts are merely transforms of each other. Shorter linewidths facilitate higher wavelength resolution in a spectrometer and more channels in a communications sys-

tems; however, it does so by reducing the maximum possible bandwidth of individual channels.

Free Spectral Range (FSR) measures the distance between each peak of a filter. Interferometers normally exhibit an infinite number of resonant modes. The distance between peaks serves as a limit on the wavelength range usable in a communications system or the possible scanning range of a spectrometer. As with linewidth, it is common to see it measured in both free space wavelength and frequency.

Finesse, the ratio of FSR to linewidth, is a common measure in communication systems as it directly pertains to the number of permissible channels: a high finesse filter has a FSR significantly longer than the passband's linewidth, allowing a large number of channels.

Contrast is the ratio of the passband maxima to the blockband minima. This affects the degree to which communication channels will be separated and the uncertainty of measure in a spectrometer. Higher contrast provides a more ideal channel separation and lower measurement uncertainty.

1.2.2 Thermooptic Effect

A common effect exploited for filter tuning is the thermoelectric effect: many materials exhibit a shift in their dielectric constant as a function of temperature. By constructing a resonant cavity of such a material, the resonant cavity can be tuned by the application of heat. Such devices are
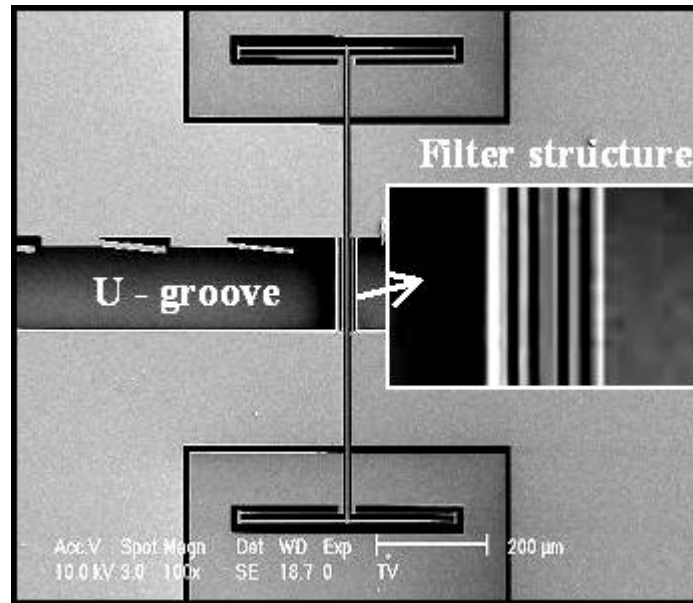
Figure 1.2: Thermooptic device with direct fiber butt coupling from [2].

demonstrated in [1, 2, 3].

The small volume of microfabricated devices lends itself well to the thermal effect in terms of time response. However, the high surface area to volume ratios of these devices require considerable amounts of power to maintain the elevated temperatures necessary. Additionally, this heat can interact with other nearby devices, restricting the density at which these devices can be spaced. In the device described in [2] (shown in Figure 1.2), 1 Watt is required to displace the passband from 1506 nm to 1513 nm with a linewidth of 1.7 to 3.4 nm. In [3], the power consumption was reduced to 83 mW for a shift of 29.1 nm with a linewidth of 0.28 nm.

The strength of the thermooptic effect is in its versatility and compat-

7

ibility with traditional microfabrication techniques. Silicon is the commonly exploited material for the resonant cavity, opening a wide variety of possible fabrication techniques and device geometries. [1, 3] make use of deposited thin films as Bragg mirrors to form an out-of-plane device while [2] utilizes plasma etching to form vertical facets for an in-plane device. As evidenced by the smaller linewidths for the out-of-plane devices, loss due to surface roughness (a key performance difference between in-plane and out-of-plane devices) is a significant factor in the performance of the plasma etched devices.

1.2.3 Electrooptic Effect

As a better substitute for the high power consumption of the thermooptic effect, the electrooptic effects are frequently exploited. A term covering multiple unrelated effects, the electrooptic moniker is used to describe any effect where the index of refraction of a material is altered through direct electrical means.

The most obvious effect, to exploit a non-linear polarization response in the material, is known as either the Kerr or Pockels effect. Polarization is normally expressed as a linear function of electric field (e.g. $P = \chi E$); however, higher order terms are generally present:

$$P = \chi^{(1)} E + \chi^{(2)} E^2 + \chi^{(3)} E^3 + \dots \tag{1.1}$$

This means that the dielectric constant (and, by extension, index of refraction) for time-harmonic waves can be tuned (to the first order) by the application of a DC field:

$$\epsilon_r^{eff} = 1 + \frac{\partial P}{\partial E}\bigg|_{E=E_{dc}} = 1 + \chi^{(1)} + 2\chi^{(2)}E_{dc} + 3\chi^{(3)}E_{dc}^2 + \ldots \quad (1.2)$$

$$n^{eff} = \sqrt{\epsilon_r^{eff}} \approx n_o + \frac{\chi^{(2)}}{n_o}E_{dc} + \frac{3\chi^{(3)}}{2n_o}E_{dc}^2 + \ldots \quad (1.3)$$

In normal crystalline materials, symmetry in the material leads to the even order terms (e.g. $\chi^{(2)}$) being zero and the coefficients are generally tensors. In these materials, where the index change is proportional to the square of the field, the effect is known as the Optical Kerr Effect. In other materials, such as glasses and fluids, the even order terms may be finite, leading to the Pockels effect, where the index shift is linearly proportional to the applied field. However, both of these effects are small in commonly microfabricated materials and the relationship is polarization dependent, limiting its utility in practice. In [4], an organic polymer serves as the resonant cavity was able to achieve a shift of 20 nm under an applied voltage of 30 V with effectively no power consumption other than the conductivity of the polymer.

Another effect commonly exploited for filters is the free-carrier plasma dispersion effect, a derivative of the Kramers-Kronig relationship relating index of refraction and absorption. As each property is a transform of the other (analogous to how position and momentum are mutual trans-
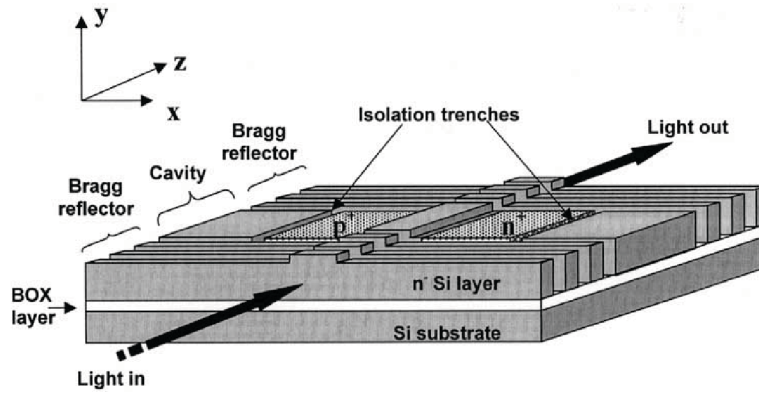
Figure 1.3: Electrooptically-tuned filter with waveguide coupling from [6].

forms in quantum mechanics), a change in one will result in a change in the other. More simply, the index of refraction is a reflection of optical loss just like wavelength is to frequency (albeit with different match). Optical loss can easily be modulated through the free-carrier effect by the injection of carriers in a PN junction. Further, since this effect does not depend on the optical properties of the material, such as bandgap or non-linear polarization constants, silicon has served as a commonly exploited material for these devices.

Devices utilizing this effect, such as those described in [5, 6], can achieve tuning significantly faster than thermal devices with significantly lower power consumption. However, the extent to which the index can be modulated is limited. In the results presented by [6], 20 mW of applied power was able to achieve a 0.8 nm shift of the center wavelength (Free Spectral Range is 17.2 nm). The cavity was the intrinsic region of a PIN diode approximately 20 μm in length, illustrated in figure 1.3.

1.2.4 Optical MEMS

A more obvious approach than altering the index of the cavity is to physically modulate its length. However, the techniques to mechanically actuate a microdevice, referred to as Micro-Electro-Mechanical Systems (MEMS), are recent. While there is no all-encompassing definition of MEMS, it is generally considered to include those devices which solve mixed-domain problems. For example, MEMS can couple the electrical and mechanical domains in the fabrication of sensors and actuators. This hybrid approach has the potential to revolutionize the capabilities of microdevices.

The use of MEMS to control optical devices has demonstrated feasibility [7, 8, 9, 10]. In [7, 8], multiple epitaxial layers of indium gallium arsenide phosphide (of different ratios) are grown on a substrate of indium phosphide to form Brag mirrors and cavities. The epitaxial structure is then dry etched to form the actual filter and various layers are wet etched as sacrificial layers to form air cavities. This structure is illustrated in Figure 1.4.

Optically, the device is composed of two Bragg reflectors around an air cavity. Actuation of the cavity is electrostatic: the cavity acts as a capacitor when a voltage is applied, depositing opposing charges which pull the opposite sides of the cavity together. This serves to decrease the cavity length and shift the passband to shorter wavelengths.

Doping the layers to form a PN junction in the main cavity minimizes leakage current. Further, it prevents any voltage drops from forming within
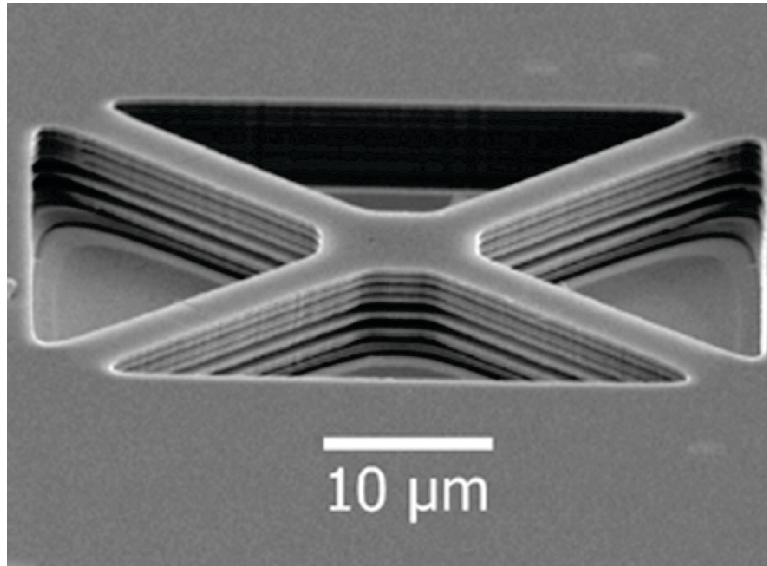
Figure 1.4: SEM of fabricated device from [8]. Light passes through the device (center of image), normal to surface.

the mirrors, which would lead to electrostatic attraction and internal deformation of the grating. Unlike the devices described in sections 1.2.2 and 1.2.3, the tuning range is immense (40 nm), limited only by the range the cavity length can be modulated and the extent of the Bragg mirror's high reflectivity band. Line width was measured at 0.15 nm, one of the best in the reviewed devices.

A similar device, fabricated in Silicon, is described in [11]. Unlike the out-of-plane coupling in [8], fiber is butt coupled to the tunable cavity as in [2]. Two third-order Bragg mirrors are suspended between the fiber core with one free to move. The application of voltage between the two mirrors induces a displacement, adjusting the cavity length. It's in-plane

design, fabricated with Deep Reactive Ion Etching (Deep RIE), leads to increased surface roughness and decreased performance compared to [8]. Line width is increased an order of magnitude to 3 nm and the tunability range is significantly decreased.

In addition to a large range of motion in the optical path length, MEMS has additional significant advantages. Unlike the thermooptic and electrooptic effects, electrostatic actuation consumes no power in static operation (excluding leakage and circuit losses). Additionally, as opposed to the Pockels and Kerr effects, the tuning mechanism introduces no additional birefringence to the system. As with the thermooptic and free-carrier plasma dispersion effects, the choice of fabrication material is largely unimportant optically, so long as it is transparent and capable of guiding. This leaves the choice of material free for other design constraints, such as availability, manufacturability, or requirements of other integrated devices.

1.2.5 Microring Resonators

While this work centers on a Fabry-Pérot-based device, it is important to consider other possibilities. Another prominent filtering technology is based on the microring resonator. Like the Fabry-Pérot interferometer, this is a resonant device; however, in this case, the resonant structure is a waveguide ring evanescently coupled to a straight waveguide, illustrated in figure 1.5. If light traveling through the straight waveguide matches a
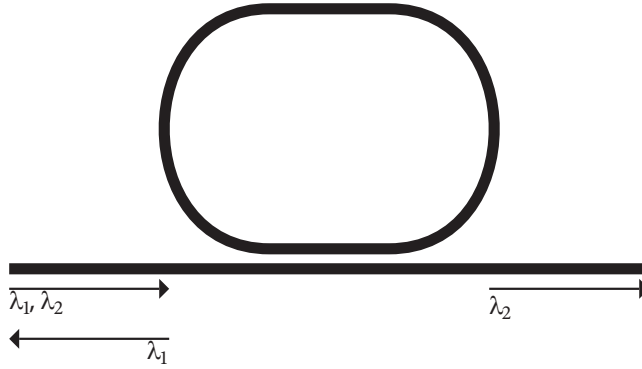
Figure 1.5: Illustration of microring resonator.

resonant mode of the microring (such as λ_1 in figure 1.5), it is reflected. All other wavelengths (such as λ_2) are transmitted. By adjusting the optical path length of the microring, the blockband can be shifted.

Microrings can be tuned in many of the same ways as Fabry-Pérot devices. For example, in [12], the electrooptic effect is used to adjust the refractive index of the microring directly. Alternatively, the properties of the surrounding environment can be adjusted, as illustrated in [13] where microfluidic channels are used to deliver mixtures of fluids with differing refractive indices.

The fully-guided properties of the microring make it a powerful tool, allowing large tunability (relative to its FSR) compared to similar techniques in Fabry-Pérot. However, microring resonators, nearly universally, have short FSR. While the linewidth achieved is extremely small, its finesse is not significantly larger than that possible with the Fabry-Pérot technique.

1.2.6 Integrated Optics

However, the majority of these devices currently operate out of the wafer plane, where light travels perpendicular to the surface of the wafer. This is not compatible with edge-emitting lasers, laser amplifiers, active optical logic, and traveling wave photodetectors. Without these features, monolithic integration with sophisticated optical logic is difficult.

Surface micromachining utilizes a sacrificial layer to produce released structures. To be effective, etch chemistries for this layer must have high selectivity versus the structural layers. However, in the case of optics, the structural layers are generally waveguides or otherwise optically significant. This further requires that the etch chemistry not attack the surface of the structural material or else the induced surface roughness may introduce significant optical loss. In the case of active optics, such as lasers, there may be multiple, chemically-distinct structural layers and etch chemistry must be selective versus all of them.

As an additional complication, the sacrificial layer, where it remains, must not interfere with the optical properties of the optically significant structures. In the case of waveguides, this means that the sacrificial layer, when serving as a cladding, must have a lower index of refraction and be non-dissipative; otherwise, the sacrificial layer will leach optical power from the waveguide. In the case of indium phosphide, indium gallium arsenide (InGaAs) serves as an effective sacrificial layer from the chemical perspective; however, it has both a higher index and smaller bandgap than
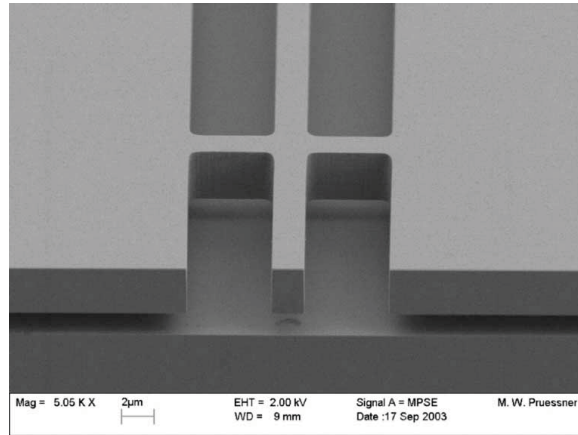
Figure 1.6: Scanning Electron Micrograph of suspended InP waveguide from [14].

indium phosphide, making it unusable as a cladding for 1550 nm light.

In [14], this problem is surmounted by suspending the waveguides. Etching all sacrificial material below the waveguide removes any possible interaction with the sacrificial waveguide, eliminating that mechanism of loss. However, the waveguide, must be supported through some means. In the case of [14], the waveguide is tethered to anchors supported by unetched sacrificial layer. A micrograph of a fabricated structure is illustrated in figure 1.6.

The waveguide tested is a square InP waveguide with a 2x2 μm core of index 3.195. It is clad on the top and bottom with 2x1 μm layers of index 3.173 material. Loss in the suspended structure is measured at 2.2 dB/cm. This is consistent with the standard bulk losses in indium phosphide, which are on the order of 0.1~1 dB/cm [15]. Furthermore, each 1.5 μm tether introduces an additional loss of 0.25 dB. As multiple millimeters of waveg-

uide can be suspended on a pair of tethers and this loss decreases exponentially with reduced tether length, the impact of the tethers can be minimized.

In the case of silicon, silicon dioxide provides a cheap and effective cladding and sacrificial layer. The index of silicon dioxide, 1.45, is significantly lower than the index of silicon, 3.42. Further, silicon dioxide's use as the primary transmission medium for 1550 nm communications establishes a reputation for low optical loss in this band. Furthermore, hydrofluoric acid (HF) provides a nearly 100% selectivity between silicon and silicon dioxide. Waveguides constructed with this choice of materials have achieved loss as low as 0.1 dB/cm utilizing commercially available Silicon-On-Insulator (SOI) wafers [16].

1.2.7 Filter Comparison

A summary of the relevant technical data from the reviewed papers is presented in table 1.1.

Most noticeable is the linewidth: out-of-plane devices [3, 8] exhibit an order of magnitude smaller linewidths than the in-plane devices [2, 6]. This expected due to the higher surface roughness suffered from anisotropic etching: In order to match the performance of an out-of-plane device, an in-plane device would need to achieve a sidewall roughness on order with the roughness achieved in the chemical deposition of thin films.

Beyond that, the power consumption of the current-driven devices [2,

Project	Technique	Material	Tuning Range	Linewidth	FSR	Finesse	Power Consumption	Integration
Yun et al [2]	Thermooptic	Silicon	7 nm	1.3 nm	Not Reported	N/A	1 W	Fiber-Coupled
Hohlfield et al [3]	Thermooptic	Silicon	29.1 nm	0.28 nm	Not Reported	N/A	83 mW	Out-Of-Plane
Gan et al [4]	Electrooptic (Pockels)	Polymer	20 nm	2 nm	470 nm	235	Not Reported	Out-Of-Plane
Barrios et al [6]	Electrooptic (Free Carrier)	Silicon	0.8 nm	1.5 nm	17.2 nm	11.2	20 mW	In-Plane
Garrigues et al [8]	MEMS	Indium Phosphide	40 nm	0.15 nm	Not Reported	N/A	Not Reported	Out-Of-Plane
Lipson et al [11]	MEMS	Silicon	8 nm	3 nm	Not Reported	N/A	Not Reported	Fiber-Coupled
Li et al [12]	Electrooptic (Microring)	Silicon	0.5 nm	0.2 nm	Not reported	N/A	Not Reported	In-Plane
Levy et al [13]	Microfluidics (Microring)	Polymer (SU8)	2 nm	0.009 nm	0.95 nm	108	Not Reported	In-Plane

Table 1.1: Comparison of reviewed C+L band (1500-1630 nm) filtering techniques.

3, 6] is considerable. In the case of [2], this is high as one Watt for a device roughly 100x10 microns. In comparison, the voltage-driven devices [4, 8] consume so little power as to not be measurable.

For the ultimate in performance, a voltage-driven out-of-plane device, such as [8], is the clear victor; however, this performance comes at a price in integration. Dense integration with active optical components will require a means by which the benefits of a design similar to [8] can produce an optical axis within the wafer plane.

1.3 Thesis

1.3.1 Objective

The primary objective of my thesis work is to design, build, and fabricate an in-plane tunable optical filter. To improve upon prior work in the field, the goal is to integrate such a device with guided optics. The vast majority of tunable devices are based on the growth of thin-films and transmit orthogonal to the wafer surface. This is advantageous for fiber coupling, but is impractical for coupling to photonic logic. If tunable filters are to be integrated into optical communications transceivers, integration with emitters and detectors is essential for maintaining a reasonable cost. The devices presented in this thesis are the first integrated mechanical filters operating with the potential for direct integration with active optics.

1.3.2 Organization

Chapter 2 introduces the basic physics behind interference filters and describes the design process that lead to the devices described in this thesis. Chapter 3 presents the fabrication of the tunable filters in indium phosphide and silicon. Chapter 4 presents the characterization system and testing results of the devices. Finally, chapter 5 summarizes the results and accomplishments of this thesis. Further, Appendix A provides a more detailed derivation of the mathematics and physics exploited in design and Appendix B provides a listing of simulation and analysis source code.

Chapter 2

Design

As described in the introduction, the principle design objective is to design and fabricate a tunable optical filter with in-plane guided optics. This chapter will present the device design and simulation results.

2.1   Basics of Fabry-Pérot Filters

The basic operation of a the Fabry-Pérot interferometer is illustrated in Figure 2.1. Light entering a cavity enclosed by partially reflective facets will become "trapped" in the cavity as it reflects back and forth. On each reflection, a small fraction of the light will "leak" out, experiencing a phase shift from its time in the cavity. The set of these transmitted rays interfere to produce an intensity modulated by the wavelength and cavity length.

Should the cavity be an integer number of half wavelengths, the phase
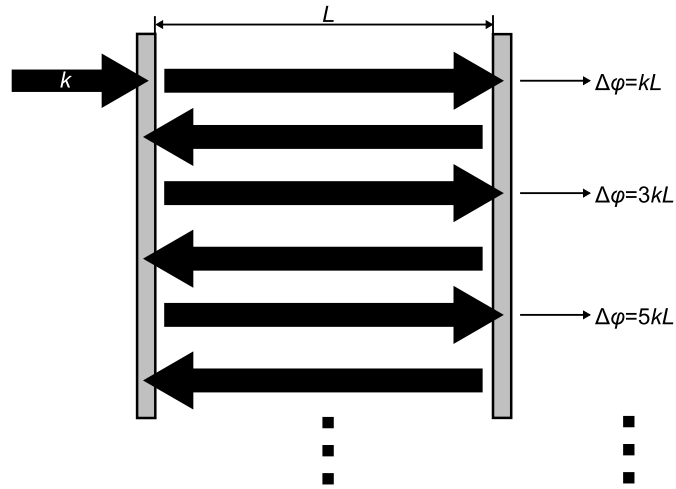
Figure 2.1: Light entering a cavity enclosed by partially reflective facets will bounce between the boundaries, transmitting some light with each reflection. Each pass through the cavity causes a phase shift.

shift of the transmitted rays will differ by 2π, leading to constructive interference and a maxima in transmitted power. Alternatively, if the cavity is an odd number of quarter wavelengths, the phase shift of the transmitted rays will differ by π, leading to destructive interference and a minima in transmitted power. An example of the output spectra is shown in Figure 2.2.

The difference between the maxima and minima transmission is termed the modulation depth and is a strong function of the cavity loss and facet reflectivity. Generally, in semiconductor devices, the reflective facets are formed exclusively from interfaces between dielectrics (semiconductor or thin film) and either air or a different dielectric (frequently a different ratio of the same tertiary compound semiconductor). However, even in an ex-
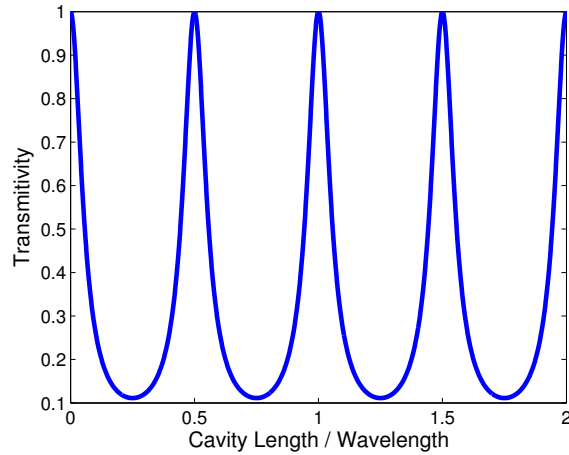
Figure 2.2: Sample response of a Fabry-Perot cavity as a function of the ratio of cavity length to wavelength. Facet reflectivity is 50%.

treme case of silicon (index of refraction 3.42) and air (index of refraction 1.0), the reflectivity is only 30%.

To increase the reflectivity of a structure, multiple quarter-wavelength plates are cascaded to form a Distributed Bragg Reflector (DBR). The effect, illustrated in Figure 2.3(a), results in an increase in reflection but a wider passband with multiple resonances. In order to increase reflection of the stopband while narrowing the peak of the passband, it is necessary to increase the reflectivity of the facets. This effect, illustrated in Figure 2.3(b), is typically accomplished by using DBRs for the facets.

23
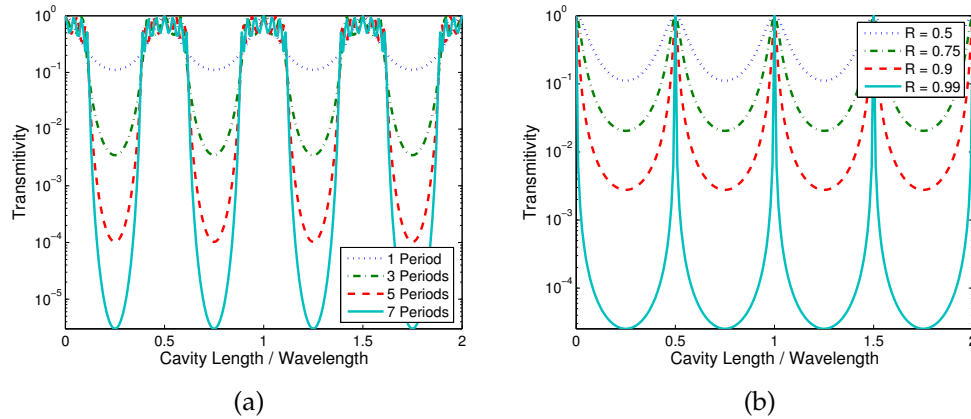
Figure 2.3: Effect on etalon optical response as a function of: (a) number of periods (facet reflectivity is 50%); and, (b) reflectivity of facets (single period). Reflectivity is 1-Transmitivity.

2.2 Design of Tunable Filter

As described in 2.1, to maximize the performance of the filter, the cavity needs to be an integer multiple of half wavelengths with a high facet reflectivity. Additionally, as the goal is to produce an in-plane device, the dimensions of each structure need to be sufficiently large as to be compatible with the limitations of projection lithography. Currently, this limits us to a minimum 0.5 μm critical dimension. Further, it is necessary to maintain a large waveguide cross-section to minimize divergence yet still provide single mode operation for compatibility with other integrated devices. Finally, we need to establish a means to tune the device.

In order to first address the issue of large, single mode structures, we investigated the use of ridged waveguides in a MEMS environment. In [17],

24

the single mode condition for a ridge waveguide is derived. In principle, the core and cladding are treated as separate, yet, coupled waveguides, each with their own mode structure derived from their geometries. In the single mode condition, the higher order modes of the core have effective indices lower than the fundamental mode of the cladding. As energy naturally "leaks" to the higher indexed modes, only the core's fundamental mode will be able to be able to propagate. In [18], this is demonstrated experimentally while making minor corrections to the design rules originally presented in [17]. Most importantly, it experimentally demonstrates that single mode operation can be sustained in waveguides of *arbitrary* size merely by controlling the ridge height.

We initially pursued indium phosphide for the filter material due to it being latticed matched with compounds of $In_xGa_{1-x}As_yP_{1-y}$ that are direct bandgap with bandgap energies in the range of 1550 μm. This allows integration of passive devices, like this filter, with active devices, such as lasers, modulators, and optical amplifiers. The layer structure we investigated is derived from [14] and is illustrated in Figure 2.4. 4 μm of material, composed of two 2 μm layers, is epitaxially grown on an iron-implanted (high resistivity) indium phosphide substrate. The top layer is indium phosphide and serves as the waveguide layer. Small concentrations of gallium and arsenic are added to induce an intrinsic tensile stress, preventing released beams from buckling. The lower layer, $In_{0.49}Ga_{0.51}P$, serves as a lattice-matched sacrificial layer as it can be selectively wet etched by an
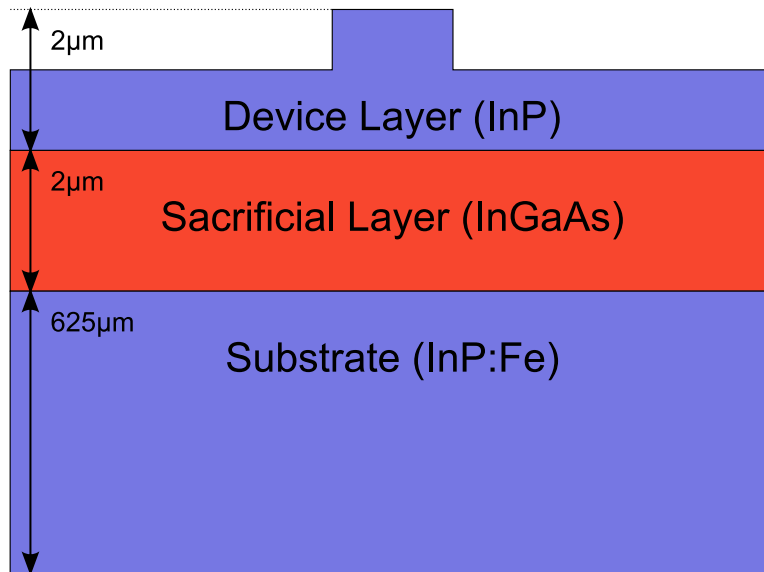
Figure 2.4: Indium Phosphide layer structure for Tunable Filter.

HF:H_2O_2 chemistry.

The waveguide thickness of 2 μm was chosen due the the MBE growing capabilities of our collaborators as well as limitations of our etch technology. A waveguide width of 2 μm was chosen to provide a square cross-section; however, this is largely arbitrary: the mode shape will dominated by the depth of the ridge. [18] provides experimentally-verified expressions for designing single mode ridged waveguides. First, a dimensional offset q representing the extent of the mode outside the waveguide is calculated from the wavelength, index of refractions, and field orientation (TE versus TM):

$$q = \frac{2\gamma}{k\sqrt{n_{wvgd}^2 - n_{clad}^2}} = \begin{cases} 162.6\,\text{nm} & TE \\ \\ 15.93\,\text{nm} & TM \end{cases}$$

$$\gamma^{TE} = 1$$

$$\gamma^{TM} = \left(\frac{n_{clad}}{n_{wvgd}}\right)^2 = \left(\frac{1}{3.195}\right)^2 = 0.09796$$

Next, the dimension offset is added to the total height (H), cladding height (h), and core width (w) to produce effective dimensions. The ratio of effective width to effective total height (t) is constrained by the ratio of effective cladding height to effective total height (r):

$$t = \frac{w_{eff}}{H_{eff}} = 1 \leq \frac{r}{\sqrt{1 - r^2}} = \frac{h_{eff}}{\sqrt{H_{eff}^2 - h_{eff}^2}}$$

Continuing the calculation for indium phosphide at 1550 nm leads to a minimum cladding height of 1.367 μm for the TE mode and a minimum height of 1.410 μm. To provide a reasonable tolerance, a cladding height of 1.5 μm (rib height of 0.5 μm) is chosen.

The index of refraction of InGaAs is larger than that of InP and the bandgap is smaller than 1550 μm; therefore, the InGaAs sacrificial layer must be etched from all waveguides or the system will suffer significant loss. To release the waveguides, a process similar to [14] is utilized. In principle, the waveguide is laterally tethered in order to suspend it once

the sacrificial layer is removed. However, large cladding regions must remain to satisfy the requirements of single mode operation, the waveguide includes 4-6 μm of cladding on each side of core. This inevitably leads to large ratios of released area to thickness, prolonging the release process.

The filter region itself is composed of a Fabry-Pérot interferometer created between two Distributed Bragg Reflectors (DBR). Given our design center wavelength of 1550 nm, the initial cavity must be an integer multiple of the half-wavelength, 775 nm. The DBRs are formed by making trenches perpendicular to the ridge through the entire device layer. To maximize the reflectivity, both the trench and the regions between the trenches must satisfy the quarter-wavelength condition. Assuming an index of 3.195 for indium phosphide, this leads to lengths of 387.5 nm in air and 121.3 nm in InP. As these scales are not manufacturable, 3 quarter wavelengths in air (1.163 μm) and 7 quarter wavelengths in InP (849 nm) are used instead; however, it is important to note that this is less ideal than quarter wave plates. Three periods of Bragg gratings are used for each mirror as this provides a maximum theoretical reflectivity in excess of 0.999 while minimizing the losses associated with side wall scattering (number of interfaces) and divergence (unguided air regions).

To tune the cavity, the mirrors need to be displaced relative to each other. To facilitate this, one mirror is suspended on a doubly-clamped beam electrically isolated from the rest of the device layer. Electrically isolated regions to the sides of the beam form a series of electrostatic ac-

tuators. Applying a voltage between the beam and an electrodes will cause the beam to displace toward that electrode. From models (to be described in Section 2.3), a length of 500 μm and width of 3 μm with a gap of 2 μm was decided upon. These values are largely arbitrary, representing a compromise between size, manufacturability, and operating voltage. Further design iterations to be fabricated include offsets in the filter line widths (-25 nm, $+25$ nm) to correct for lithographic errors, multiple cavity lengths (half and full wavelength), and alternative actuator designs. However, as this beam must be fully free in order to actuate, this introduced a second cavity between the moving mirror and output waveguide, visible in the final design illustrated schematically in Figure 2.5.

2.3   Modeling

While the design corresponds to the simplified descriptions in Section 2.1, it's important to verify the design's behavior to more sophisticated models. A variety of assumptions and simplifications were made in the design process, out of necessity, so it is imperative to validate them

Additionally, given the fabrication complexities eventually apparent, it is desirable to study how the device is expected to behave in other materials, namely, Silicon-On-Insulator (SOI). As silicon is easier to machine, it provides an opportunity to more easily demonstrate the device in a manner which is still directly applicable to active bandgap materials. For pur-

29
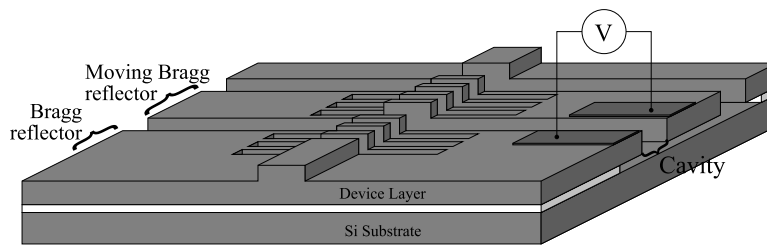
(a) Perspective view of filter
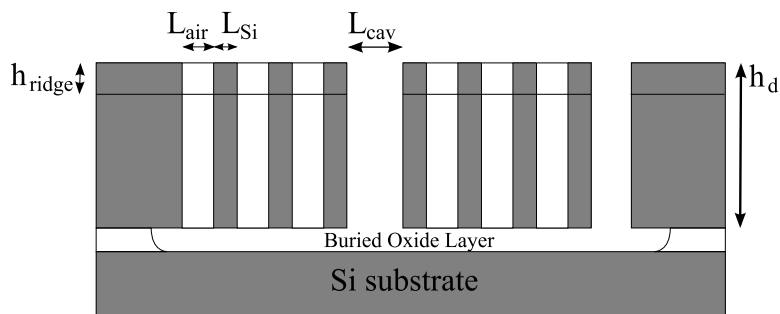
(b) Cross-section of filter. Propogation direction is to the right.

Figure 2.5: Tunable optical filter based on a Fabry-Pérot interferometric microcavity with Bragg reflectors in a single-mode Silicon ridge waveguide. The center wavelength of the filter is controlled by the application of voltage between the central, movable Bragg reflector and the device layer to either side.

poses of material availability, the device layer thickness in the silicon devices is increased to 4 μm and the maximum ridge height is increased to 1.5 μm ($r = 0.625$) while all lateral dimensions remain unchanged. This is an optically passive device, so the choice of material is not as significant in the device design (excluding length changes due to differences in refractive index).

2.3.1 Waveguides

In order to properly model the device, it is necessary to study the propagation parameters of the waveguide. Given the complex geometry of a ridge waveguide, analytical models only provide coarse approximations. To study this more fully, the waveguide cross-section was modeled in the perpendicular propagation model in COMSOL Multiphysics 3.3's RF module. In this model, the eigenvalues of the wave equations (harmonic formulation) for electric and magnetic fields are found in order to provide the modal energy distributions and propagation constants for a specific waveguide geometry.

In indium phosphide, the fundamental TE mode for 1550 nm (illustrated in Figure 2.6), has an effective index of 3.1619 and the fundamental TM mode has an effective index of 3.1666. Equivalent analysis for the silicon waveguides yields an effective index of 3.4072 for the TE mode and 3.4084 for the fundamental TM mode. These numbers are within 1% of the bulk index of refractions. This is unsurprising as due to the large in-
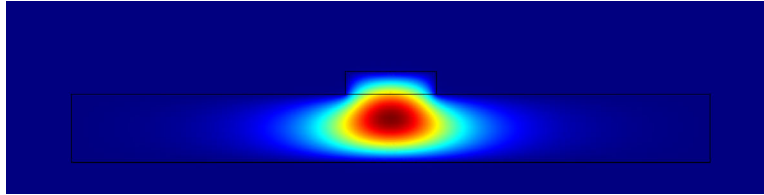
Figure 2.6: Plot of fundamental mode (TE) shape in Indium Phosphide ridged waveguide. Effective index is 3.1619. Core size is 2x2 μm. Ridge height is 0.5 μm.

dex difference between these materials and the cladding (air), the majority of guided energy remains within the waveguide. Further, it supports the use of bulk values in the design process: tolerances for the dimensions of fabricated devices will dwarf the variation between bulk and guided indices.

While the loss due to free carrier absorption and other effects can be simulated, these effects will be orders of magnitude smaller than those produced by fabrication error and etching-induced sidewall roughness. Furthermore, due to the use of fully guided optics, any distributed propagation loss significant enough to measurably effect filter performance would also leave the waveguides unusable for device interconnection.

2.3.2   Filter Static Characteristics

As DBRs and Fabry-Pérot interferometers are one-dimensional photonic bandgaps, the designs were modeled using the well established transfer matrix method described in appendix A. Assuming we couple only

with the fundamental mode and there is no exchange of energy between waveguide modes, we approximate the system as two waves: one propagating in the $+z$ direction with propagation constant and field distribution of the fundamental mode, and an equivalent wave propagating in the negative $-z$ direction. By advancing phase in guided regions and exchanging energy at interfaces according to the Fresnel coefficients, it becomes trivial to construct a linear system of equations describing the optical transfer function of the system. The computed effective index of refractions for the TE mode were used in these calculations for both propagation and reflection. Quantitative data was extracted from the simulations by performing a nonlinear least squares fit of to a Lorentzian over the range of wavelengths from 1520 to 1630 nm.

For indium phosphide devices, this method calculates a center wavelength of 1541.8 nm and a full-width half-max of 0.0576 nm. For silicon devices, this calculates to a center wavelength of 1602.0 nm and a full-width half-max of 0.0429 nm. Despite using dimensions intended for the lower index of indium phosphide, the improvement in the linewidth of the silicon device is attributed to the greater Fresnel reflectivity of silicon due to its higher index. The shift of the central wavelength is due to a phase error in the Bragg mirrors for silicon at 1550 n, leading to an effective phase shift in reflections from the mirrors. Use of the -25 nm linewidth correction improves the phase condition of the Bragg periods, shifting the center wavelength of the silicon devices to 1579.2 nm and further decreases

the linewidth to 0.0366 nm. The presence of the back cavity was a subject of initial concern; however, the model indicates this induces a shift of less than 0.1 nm in the central wavelength and a decrease in linewidth of 0.012 nm in the silicon devices. The improvement in linewidth from the back cavity is due to the additional facets, effectively increasing the number of periods in the grating and its overall reflectivity.

However, this model ignores the two primary loss mechanisms at play in the system: divergence and interface scattering. Anisotropic plasma etching, such as that required to produce a practical guided optical waveguide, leaves considerable surface roughness. The effects of surface roughness have been studied extensively for use in the development of solid states lasers and is treated theoretically in section A.4 of the appendix. In summary, the interface is treated as a continuum of scattering sites for Huygens diffraction. Due to roughness, each scattering site introduces a relative phase shift dependent on how far is displaced from a planar interface. Assuming standard Gaussian roughness, this corresponds a Gaussian distribution of phases with deviations:

$$\Delta\phi_{transmit} = \Delta d \cdot \left[k_{left} - k_{right} \right]$$

$$\Delta\phi_{reflect} = 2 \cdot \Delta d \cdot k_{left}$$

where Δd is the RMS roughness, k_{left} is the wavevector of the incident wave, and k_{right} is the wavevector of the transmitted wave. Integrating
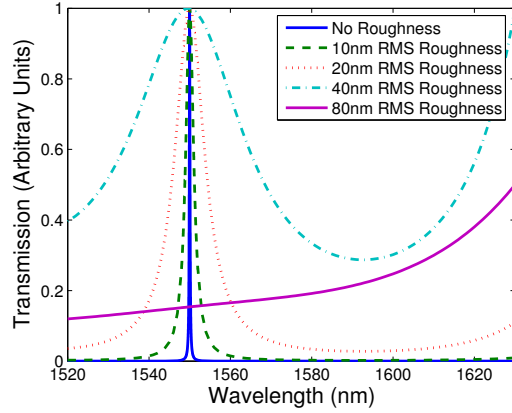
Figure 2.7: Simulation of effect of sidewall roughness on filter performance

phase over the distribution leads to scaling factors for both reflection and transmission:

$$r' = r \int\limits_{-\infty}^{+\infty} \frac{1}{\Delta\phi\sqrt{2\pi}} e^{-\phi^2/2\Delta\phi^2} e^{i\phi} d\phi = r \cdot e^{-\left(2\cdot\Delta d \cdot k_{left}\right)^2/2}$$

$$t' = t \int\limits_{-\infty}^{+\infty} \frac{1}{\Delta\phi\sqrt{2\pi}} e^{-\phi^2/2\Delta\phi^2} e^{i\phi} d\phi = r \cdot e^{-\left(\Delta d \cdot \left[k_{left}-k_{right}\right]\right)^2/2}$$

The inclusion of these expressions into the transmission matrix formulation for the Indium Phosphide design leads to the results illustrated in Figure 2.7. (Program listing available in section B.1.) Clear from the figure is that beyond a certain roughness threshold, the loss in the filter is too great to sustain proper device operation. In order to achieve a line width of 2 nm, the line width expected from losses due to divergence alone, surface roughness on the order of 10 nm is required.

35

2.3.3 Tunable Filtering

The filter is tuned by mechanically modulating the length of the cavity. The position of the moving mirror, resting on a doubly-clamped beam can be computed by the application of the Euler-Bernoulli beam equation and simple electrostatics. The beam and side electrodes form a capacitor, leading to an approximately uniform electric field of V/d normal to the surface and a surface charge density of $\varepsilon_o V/d$ in air, where V is the applied voltage and d is the distance between the electrodes. For small displacements, this corresponds to a surface load of $\rho_s E_n$ normal to the surface:

$$F_n = \varepsilon_o \frac{V^2}{d^2}$$

It should be noted that the direction of the force is independent of the voltage sign. Negation of voltage leads not only to an anti-parallel field, but also negation of the surface charge. Therefore, this force is always attractive.

Application of the Euler-Bernoulli beam equation to a doubly clamped beam of length L, width w, uniform surface load F_n, Young's modulus E, and rectangular cross-section leads to a maximum displacement at the center of:

$$u_{max} = \frac{F_n L^4}{32 \cdot E \cdot w^3} = \frac{\varepsilon_o V^2 L^4}{32 \cdot E \cdot w^3 d^2}$$

The expression is independent of thickness to the first order: both total

force and displacement are linear functions of thickness. To higher orders, a small ratio of thickness to gap will lead to a significant portion of the electric field distributed in fringing fields, reducing the force applied to the beam. This is, in part, countered by displacement decreasing the gap, increasing the electric field and, by extension, the force on the beam. For a 6.9 μm wide (3.5 period), 500 μm long indium phosphide beam with a 1.5 μm gap (as utilized in the design), this corresponds to displacements of 13.7, 54.7, and 123.2 nm for 5, 10, and 15 Volts respectively. As the Young's modulus of silicon is roughly twice that of indium phosphide and the relationship between voltage and force is quadratic, the silicon devices will require roughly 1.4 times as much voltage for the same amount of tuning.

However, as illustrated by the effect of index on the center wavelength in the previous section, the center wavelength is not necessarily equal to the cavity length. While the Bragg mirrors retain their high reflectivity off of the quarter wave condition, the composite reflectivity becomes complex, introducing a phase shift. This effect can be trivially calculated using the same methods utilized for the static case.

Simulation results for the 500 μm long, 6.9 μm indium phosphide beams are shown in figure 2.8. The rest position has a center wavelength of 1550 nm (assuming no lithographic errors). The tuning is highly linear with cavity elongation, corresponding to a shift of 0.40 nm per nanometer of displacement. Applying the electrostatic model, this corresponds to

(a) Center Wavelength as a function of (b) Center wavelength as a function of
Change in Cavity Length   Applied Voltage
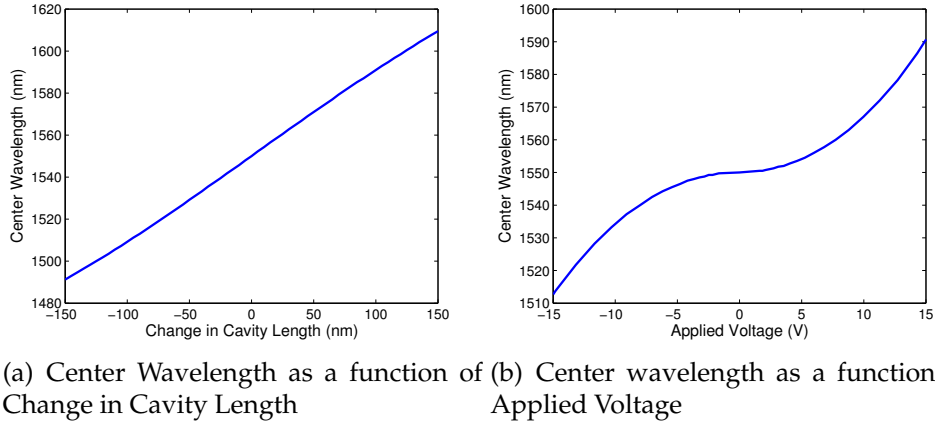
Figure 2.8: Plot of simulated passband center for 500 μm indium phosphide devices. Sign of voltage on (b) refers to set of electrodes used (to enlarge or shrink the cavity), not the polarity applied.

approximately 0.3 nm of tuning per applied Volt (near 0).

Further consideration is given to the length of the cavity: a cavity mode is supported for each wavelength that is an integer division of twice the cavity length. The distance, in wavelength, between two cavity modes is known as the Free Spectral Range (FSR). In order to ensure only one mode exists in the region of interest, the FSR must exceed the entire tuning range. If we define the tuning range as the entire high-reflectivity band of the 7/4 order Bragg mirrors, this corresponds to a maximum of two and a half wavelengths (3875 nm). There is a practical limit to cavity length beyond FSR: as the cavity is unguided, longer cavities increase the energy loss to beam divergence, broadening the line width.

Chapter 3

Fabrication

Two separate material systems were explored in the development of the filter: silicon and indium phosphide. For long term integration, indium phosphide is the more interesting material owing to its direct bandgap and extensive material system. However, plasma tools to provide smooth etches in III-V's are less commonly available than those for silicon, let alone issues of material availability and cost. This leads to the simultaneous study of both systems, silicon to provide a window to performance at low levels of roughness and Indium Phosphide in the interest of long-term application.

(a) 6000 Å oxide hard mask is deposited and patterned for rib etch

(b) 0.5 μm RIE etch is performed to define rib

(c) 6000 Å oxide hard mask is deposited and patterned for facet etch

(d) 2 μm (device layer thickness) RIE etch is made to define facets

(e) Layer structure of Ni:Ge:Au:Ni:Au is evaporated over patterned resist and lifted off to form contacts

(f) Structure is sacrificially released in HF:H_2O_2:H_2O, and device is supercritically dried

Figure 3.1: Fabrication process flow.

3.1 Indium Phosphide Process

The process for fabrication of indium phosphide MEMS devices has been well developed in prior work [9, 14, 10, 19]. This process has been extended to include an initial shallow etch to define the optical waveguides and is illustrated in figure 3.1.

Each device is processed at the die level. The initial wafer has an initial 6000 Å of oxide deposited by HDPECVD and will is cleaved into
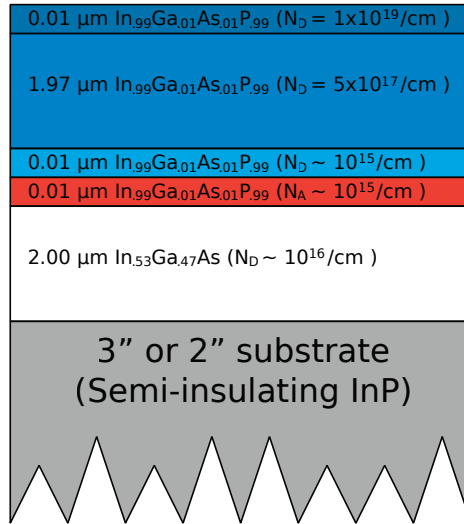
Figure 3.2: Layer structure of indium phosphide devices.

die for processing. These die are then patterned and etched 0.5 μm to form the ridge waveguides. The etch process is then repeated through the wafer with a different pattern to form the optical facets forming the resonant cavities and mechanical structures. A metal layer structure of Ni:Ge:Au:Ni:Au is then evaporated and pattern using metal lift-off. Finally, the die is thinned, cleaved, chemically released, and dried for testing.

The layer structure for the indium phosphide is illustrated in figure 3.2. It is composed of a 2 μm InP device layer grown on top of a 2 μm standard InGaAs layer on a Fe-doped semi-insulating InP substrate. The top 100 Å of the device layer is highly doped to facilitate the formation of an ohmic contact while the bottom 200 Å is composed of an n- and a p-type layer

41

Parameter	Value
SiH_4 (100%) gas flow	4 sccm
N_2O gas flow	20 sccm
RF power	4 Watts
ICP power	500 Watts
Temperature	300 °C
Time	300 s

Table 3.1: SiO_2 deposition parameters

to form a P-N junction in the goal of minimizing leakage. Furthermore, minute, stoichiometric concentrations of gallium and arsenic are added to the device layer in order to introduce intrinsic stress as well as correct for the inevitable diffusion of arsenic from the sacrificial layer.

3.1.1 Etching

All features are etched with the same process. First, 6000 Å of silicon dioxide are deposited on the sample in an Oxford System 100 High-Density Plasma-Enhanced Chemical Vapor Deposition (HDPECVD) system using the parameters in table 3.1. OiR 906-10, a positive high-contrast one-micron thick resist, is then spun at 3000 rpm and soft baked at 90 °C for 1 minute. The resist is patterned in a GCA ALS Waferstep 200 5X projection lithography system, hard baked at 120 °C for 1 minute, and developed in OPD 4262 for 1 minute. The pattern is transferred into the hard mask in a Plasmatherm 790 Series RIE with an SF_6-based chemistry. Afterwords, the resist is stripped in an asher and the actual etch process begins.

Parameter	Value (Etch)	Value (Clean)
CH_4 gas flow	8 sccm	
H_2 gas flow	32 sccm	
O_2 gas flow		19 sccm
RF power	440 Watts	200 Watts
Time	5 min	3 min

Table 3.2: Indium phosphide etch parameters
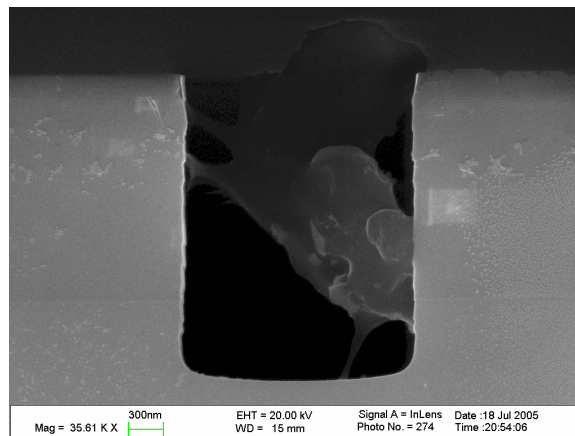
Figure 3.3: SEM of etched indium phosphide sidewall.

The actual etch chemistry is described in [20], consisting of alternating phases of $CH_4 - Ar - H_2$ and O_2 using the parameters detailed in table 3.2. The methane chemistry serves as the primary etch component while the oxygen step cleans the various polymers formed during the etch. As shown in figure 3.3, the sidewall is quite rough with a surface roughness on the order of 50 nm.

43

3.1.2 Metalization

The contact pattern is made in NR7-1500PY, a negative 1.5-micron thick photoresist, using the same 5X optical stepper and bakes as the etch pattern. The metal structure of Ni:Au:Ge:Ni:Au (50:800:400:300:2000 Å) is blanket deposited in a CHA Industries Mark 40 electron beam evaporator over the sample. The photoresist is then dissolved in a solvent (Resist Remover 2 from Futurrex, Inc.) for lift off.

The final metal structure is annealed for 60 seconds at 400 °C in forming gas ($N_2 - H_2$) in a Metron Technology AG Heatpulse rapid thermal annealer to form the ohmic contacts. This forms an alloy of germanium and gold as the actual contact material while the nickel layers consume native oxides to improve adhesion and electrical conductivity.

3.1.3 Final Preparation

Prior to release and mounting, the sample needs to be cleaved in order to provide atomically smooth facets for fiber coupling. This process begins with the sample being thinned to 200 μm on a lapping machine using a slurry of water and 9 micron alumina particles. Afterwords, cleave lines are etched into the sample's top surface with a pulsed laser and the sample is cleaved across a layer blade. Each individual "subdie" is then ready for release and testing.

The sacrificial layer is etched with a solution of $H_2O:H_2O_2:HF$ (8:1:1).
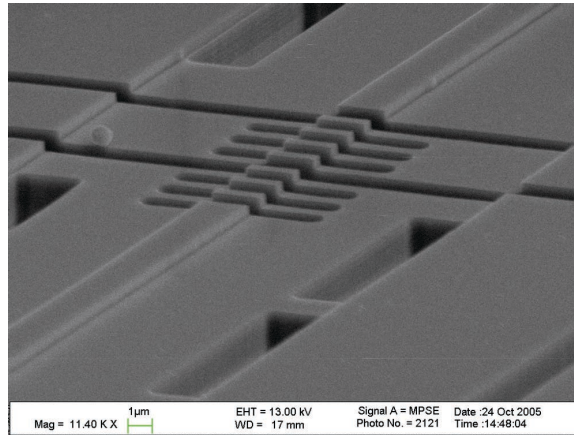
Figure 3.4: SEM of fabricated indium phosphide device.

This etches at a lateral rate of approximately 1 μm/min and has extremely high selectivity between InP and InGaAs with no apparent surface roughening or attack on InP. The sample is left in alcohol (methanol or isoproponal) until it is supercritically dried in CO_2 to prevent stiction. Afterwords, it is mounted on an aluminum boat by double-sided tape.

An SEM of the fabricated device is shown in figure 3.4.

3.2 Silicon Process

The most significant consideration, as established in the modeling section, in the fabrication is the sidewall roughness. In order to achieve the necessary level of smoothness, we make use of a M0RI etcher. Magnetic zero resonant induction (M0RI), as described in [21], has been used extensively in the compound semiconductor industry for smooth, highly vertical side-

walls. By coupling an ICP source with rare earth permanent magnets and electromagnets, helicon waves increase the plasma charge density an order of magnitude over standard ICP. The M0RI used by this project is used in production of silicon-based devices, gas availability and concerns over contamination on the part of the owner limited us to compatible materials. When processing silicon, the machine is capable of simultaneously growing a passivation layer while etching. This allows even higher aspect ratios than the common Bosch (Deep RIE) process without the indicative scalloping; however, maximum depth is much more limited and stable etch chemistry is considerably more sensitive to variations in loading.

The fabrication process is illustrated in figure 3.5. The layer structure is conceptually similar to indium phosphide, with discrete device and sacrificial layers. Full 6″ (150 mm) Silicon-On-Insulator (SOI) wafers with a 4 μm device layer and 2 μm buried oxide layer are processed in fabrication instead of individual die. The use of 6″ wafers is for compatibility with the M0RI, a production tool.

3.2.1 Through Etch

Due to the increased depth of the rib etch, it is impossible to spin a uniform layer of resist and pattern the mirror facets across the rib; therefore, the rib and through etches are reversed from the indium phosphide process. The etch process begins with the blanket deposition of 1 μm of silicon dioxide on a pristine SOI wafer in a Trion PECVD using the parameters in table 3.3.

(a) 2000 Å oxide hard mask is deposited and patterned for rib etch

(b) 1.5 μm M0RI etch is performed to define rib

(c) 2000 Å oxide hard mask is deposited and patterned for facet etch

(d) 4 μm (device layer thickness) M0RI etch is made to define facets

(e) 2000 Å of aluminum is deposited and patterned to form contacts

(f) Structure is sacrificially released in HF, aluminum resist pattern is stripped, and device is supercritcally dried

Figure 3.5: Fabrication process flow.

Parameter	Value
SiH$_4$ (2%) gas flow	400 sccm
N$_2$O gas flow	200 sccm
RF power	70 Watts
Pressure	750 mTorr
Temperature	300 °C
Time	490 s
Measured Thickness	10550 Å ($\pm$4%)

Table 3.3: SiO$_2$ deposition parameters

Parameter	Value
Ar gas flow	90 sccm
C_4F_8 gas flow	30 sccm
C_2F_4 gas flow	30 sccm
M0RI coil power	2500 Watts
Platen power	450 Watts
Pressure	5 mTorr
Temperature	-20 °C
Inner coil current	60 Amps
Outer coil current	60 Amps

Table 3.4: M0RI parameters for the hard mask etch.

This film has full-wafer thickness uniformity on the order of 4% and an index of 1.45.

To pattern the hard mask, a layer of HMDS is spun at 3000 rpm for 60 seconds followed by a layer of OiR 906-10 at 600 rpm for 60 seconds. The resist is soft baked at 90 °C for 60 seconds with a measured thickness of 0.92 μm. It was patterned in a GCA ALS Waferstep 200 using the same mask as the InP rib etch. Exposure parameters were 0.128 seconds with a focus correction of -2; however, as with all parameters, these are device and pattern specific. After development in OPD 4262 for 90 seconds, the wafers are hard baked at 120 °C for 60 seconds, and then baked in an oven at 105 °C for 30 minutes to harden the resist prior to etching.

The facet pattern is transferred into the hard mask using the M0RI. This recipe was an Ar-C_4F_8-C_2F_4 chemistry (parameters listed in table 3.4) with end-point detection. Argon serves as the primary etch component (ion milling) while the fluorocarbons serve to polymerize the resist into
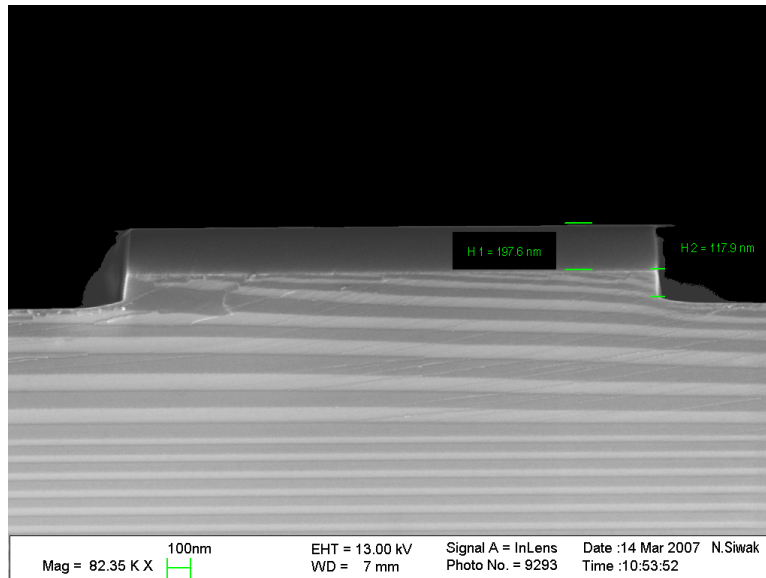
Figure 3.6: Cross-sectional SEM of patterned SiO_2 hard mask.

a Teflon-like material in order to improve selectivity. This etch produces an extremely smooth, vertical etch in the oxide, visible in figure 3.6. The lack of selectivity of the Ar-dominated etch is demonstrated by significant etching into the silicon substrate. After the hard mask is patterned, the chamber is O_2 cleaned to remove any sidewall organic contamination and the resist is stripped in a dedicated O_2 ashing unit attached to the M0RI cluster tool.

The etch itself is performed in the M0RI with a $SF_6 - SiF_4 - HBr - O_2$ chemistry (parameters listed in table 3.5). SF_6 and HBr serve as the primary etch components with SiF_4 providing additional fluorine radicals. O_2 reacts with the silicon-containing byproducts of the etch to passivate the sidewalls with a layer of a silicon dioxide passivation. In situations

Parameter	Value
SiF$_4$ gas flow	70 sccm
SF$_6$ gas flow	52 sccm
HBr gas flow	25 sccm
O$_2$ gas flow	35 sccm
M0RI coil power	2500 Watts
Platen power	40 Watts
Pressure	20 mTorr
Temperature	-20 °C
Inner coil current	60 Amps
Outer coil current	60 Amps

Table 3.5: M0RI parameters for the silicon etch.

where the aspect ratios lead to a deficiency of silicon, SiF$_4$ contributes additional silicon for oxidation. Etch time was 40 seconds for an expected etch depth of 2 μm.

An SEM of the etched facet is shown in figure 3.7. While roughness is visible under direct viewing, it is below the resolution of the SEM in profile. However, the surface quality is uneven along the depth of the sidewall. Towards the top of the sidewall, a long continuous notch is etched to a depth of approximately 75 nm falling off to unmeasurable levels. Unfortunately, notch formation was largely unaffected by process parameters and attempts to eliminate it were unsuccessful. Given the limited spatial extent, the optical impact should be minimal.
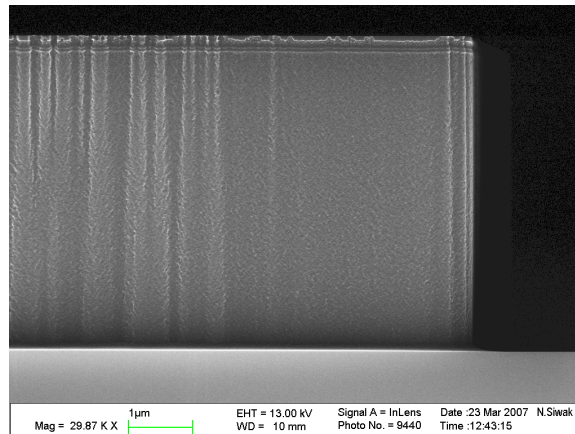
Figure 3.7: SEM of ridge sidewall. Sidewall passivation has not been removed.

3.2.2 Rib Etch

The rib etch reuses the hard mask from the through etch. A second pattern is etched into the remaining oxide and etched using the same process. The silicon etch process uses the same process parameters with an etch time of 31 seconds for an expected etch depth of 2.0 μm.

In addition to forming the rib, the logical AND of the two patterns resulting from sharing the hard mask makes it responsible for dropping the through-etches to the oxide. Overetching is dangerous due to charging of the silicon layer by the etching radicals: this leads to footing as the embedded charge in the oxide deflects incoming ions. In the final SOI fabrication, the etch was 510 nm short of the desired depth, illustrated in figure 3.8. As measuring this depth involves cleaving the wafer, additional etching waited until after the wafer diced (explained below). Once the etch
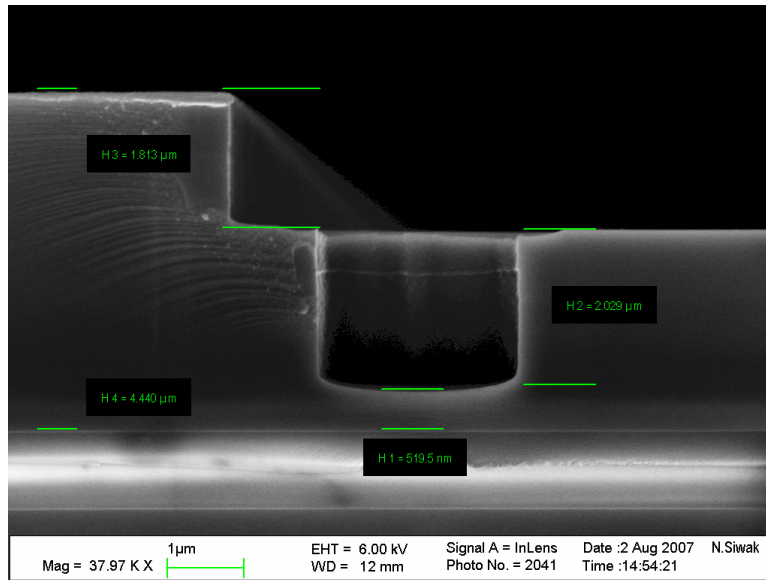
Figure 3.8: Cross section of etched SOI device illustrating insufficient etch depth.

depth was determined, individual die from the diced wafer were stripped of the hard mask in 40% HF, mounted on a 6″ silicon carrier with thermal paste, and blanket etched in the M0RI for 15 seconds.

3.2.3   Dicing

As the SOI devices were produced on the wafer-level, unlike the InP devices, it is necessary to dice the wafer into individual die prior to testing. Ordering of these final processes is important: As it is unknown during dicing if the rib etch has broken through to the buried oxide. Further, early process development found the combination of silicon saw dust and water cooling used by the dicing saw was destructive to the metal contacts. For

these reasons, die are metalized individually after dicing.

The wafer is first spun with a thick layer of Microposit (~20 μm) for physical protection. It is then backed by a plastic sheet and diced into 14x14 mm die on a Disco DAD-100 automated dicing saw. Individual die can then be removed from the backing sheet and the Microposit layer is removed in acetone as part of a standard rinse.

3.2.4   Aluminum Deposition

Due to use of a SiO_2 sacrificial layer, the contact metal needs to survive an HF sacrificial etch. Aluminum on p-type material is a highly effective ohmic material; however, it will etch in HF as rapidly as SiO_2. To combat this, the metal lift-off technique used for indium phosphide was replaced with a masked chemical etch in commercial aluminum etchant (end point visually inspected), leaving the resist mask intact during release to protect the contacts. As with the metal stack in indium phosphide, the aluminum layer is deposited in a CHA electron beam evaporator.

3.2.5   Final Preparation

The finished die is sacrificially released in 40% HF. This process exhibited a significantly slower etch rate than the equivalent process in InP, relying on optical inspection of release indicators for etch timing. It is likely residues of photoresist from metalization interfered with the diffusion of
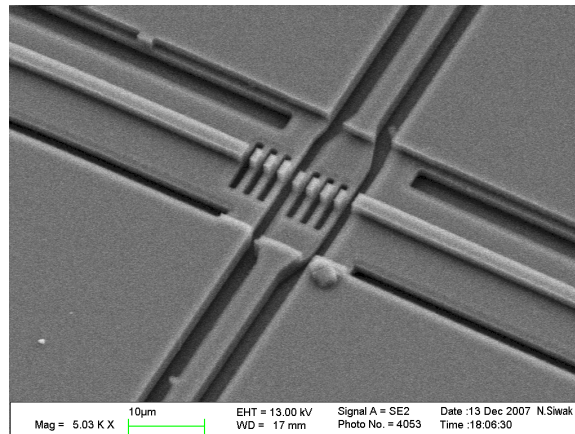
Figure 3.9: SEM of fabricated Silicon-On-Insulator filter. Visible in this device is stiction to the substrate.

etchant to the sacrificial layer; however, such protections did not aid the aluminum contacts. Attempts to descum the photoresist as well as over-expose during metal patterning proved unable to address this problem. In the end, the contacts were abandoned and use of direct probing of silicon was planned. This would impair high-speed dynamic operation, but not effect low-frequency operation as electrostatic tuning is capacitive in nature.

After release, the die are washed in DI (to remove any HF) and Acetone (to remove any left-over resist) and subjected to the same super-critical drying as per indium phosphide. An SEM of a completed SOI device is illustrated in figure 3.9. The filter visible in the SEM is suffering from stiction to the substrate, an issue affecting silicon devices more frequently than indium phosphide devices. This is initially surprising, considering silicon's higher Young's modulus would lead one to conclude silicon de-

54

vices would be less susceptible to stiction. However, it is not unexpected given residues interfering with the release process and the hidden challenges encountered when deviating from the established fabrication process our group developed for indium phosphide. While this produces a measurable impact on yield, the considerable quantity of devices manufactured on a single wafer (approximately 90 die) mitigates this issue.

Chapter 4

Testing

4.1 Measurement System

Being an optical filter, the primary issue for characterization is its optical transfer function. Assuming a passive system, this can be studied by probing with a narrow band source and measuring intensity as a function of input intensity and wavelength. The ratio of output to input intensity versus wavelength provides a measure of $|H(\omega)|^2$. A system for measuring this relationship is illustrated in figure 4.1.

The basic principle of operation is to introduce a probe signal of known (ideally monochromatic) spectrum then measure the optical power of the transmission through the device. Being a linear optical system, this is conceptually equivalent to being the physical realization of the mathematical processes described in section 2.3.2. In the case of a tunable polychromatic
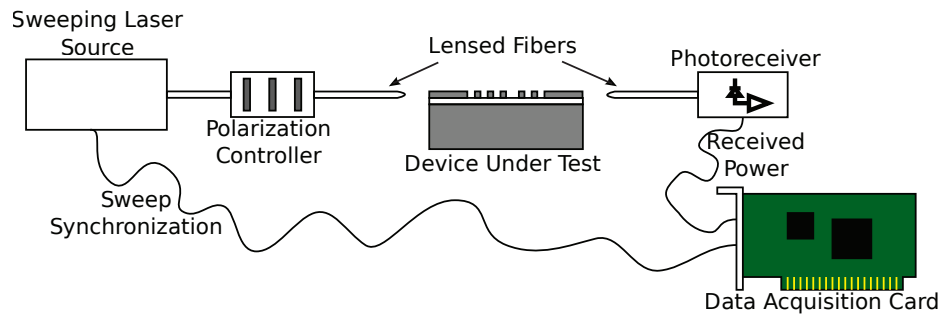
Figure 4.1: Schematic of system for characterization of optical devices. A tunable source sweeps across the range of wavelengths while a computer records the transmission as a function of time and synchronizes it to the laser.

source, the same information could be extracted via deconvolution of the two spectra, but that is beyond the scope of this discussion.

The most direct implementation of the principle described above is to tune a laser source to a specified wavelength and then make a power measurement, iterating through the spectrum; however, this technique is impractical and the time required for discrete stepping leads to a variety of complications. Most importantly, drift in the tunable source and stages aligning the fibers to the device lead to significant sample-to-sample uncertainty. In order to minimize this uncertainty, it is necessary to minimize the time between any two points on the spectra.

Our test laser, a New Focus TLB-6600 Venturi Tunable Laser, is capable of a continuous sweep through its operating range of 1520-1630 nm at rates of 2-2000 nm/s. At a "conservative" sweep speed of 200 nm/s, the entire spectrum can be covered in 0.55 seconds. Furthermore, a digital syn-

chronization signal is generated at the beginning of each sweep. By using this signal to trigger data collection on an oscilloscope or Data Acquisition Card (DAQ), the intensity versus wavelength can be easily reconstructed after each scan.

4.2   Indium Phosphide Devices

4.2.1   Waveguides

Prior to testing the optical components, loss in the waveguide is measured. This relies on the same basic principle of the filter: Fabry-Pérot interference between the facets of the waveguide. Originally described in [22], this method has significant advantage over other techniques: it does not depend on repeatable coupling, absolute accuracy improves as loss decreases, and the test is non-destructive while being simple to perform. An example scan of a 2 μm rib waveguide with 6 μm of cladding and 4 4 μm tethers is shown in figure 4.2. As transmission varies across the spectrum (likely due to wavelength-dependant coupling and losses), analysis of loss will occur within short bands of wavelength. Such an analysis leads to the plot in figure 4.3 with average loss of 2.25 dB or 7.5 dB/cm. This method, continued onto multiple combinations of tethers and claddings leads to the results in table 4.1. (Source code is available in section B.2 of the appendix).
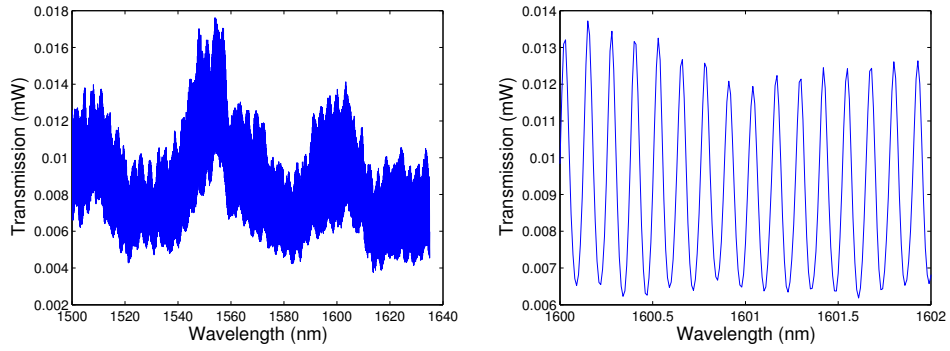
(a) Entire measured spectral response   (b) Zoom of response from 1600-1602 nm

Figure 4.2: Transmission through a 3mm long ribbed waveguide (2 μm core, 4 4 μm tethers).
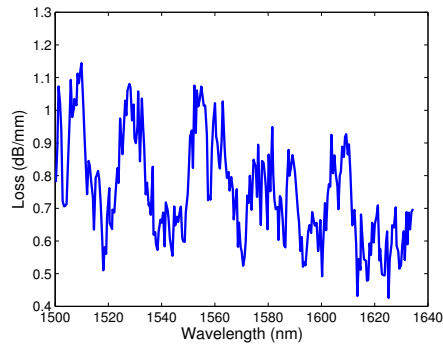
Figure 4.3: Loss through a 3mm long ribbed waveguide (2 μm core, 4 4 μm tethers).

Geometry		Measured Loss			
Tether Width	Cladding Width	2 Tethers	3 Tethers	4 Tethers	Average
2 μm	4 μm	2.75 dB	2.51 dB	1.57 dB	7.7 dB/cm
2 μm	6 μm	1.67 dB	Damaged	1.50 dB	5.3 dB/cm
4 μm	4 μm	2.15 dB	1.54 dB	1.59 dB	5.9 dB/cm
4 μm	6 μm	1.53 dB	1.84 dB	2.13 dB	6.1 dB/cm
5 μm Periodic	6 μm	2.76 dB			9.2 dB/cm
10 μm Periodic	6 μm	1.93 dB			6.4 dB/cm
15 μm Periodic	6 μm	1.71 dB			5.7 dB/cm

Table 4.1: Waveguide loss measurements.

An important consideration is the effect of the support structure (tethers) on light propogation. As evident in table 4.1, there is no clear relationship between the geometric properties of finite tethers and loss. Except in the case of 4 μm tethers with a 6 μm cladding, loss tends downwards with increasing numbers of tethers. In this case, we could estimate a loss of 0.3 dB/tether and 3.1 dB/cm of waveguide. However, it's clear an external influence dwarfs any contribution from these structures. Possibly reasons include fabrication uncertainty and wavelength-dependance on the tether losses. The loss is consistant with the 2.2 dB/cm for a square waveguide presented in [14], but can not be directly compared due to the different waveguide geometries: higher surface area and core volume leads to increased loss, placing increased dependance on the etch quality.

Unlike [14], however, we have the tools to examine the power cross-section of the waveguides. Illustrated in figure 4.4, is the measured power versus linear displacement of the output fiber while optical power is still
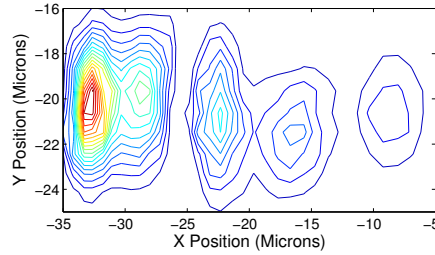
Figure 4.4: Power cross-section of a suspended ridge waveguide with 6 μm cladding and 4 μm tethers.

coupled into the fundamental mode. As expected, the highest intensity of optical power is in the waveguide core (centered at x=-33 μm, y=-20 μm), but additional local maxima of power are visible. Each of these correspond to higher order modes in the waveguide. The mode centered at x=-28 μm is one node of the second-order mode, while the modes further to the right are modes carrying energy lost through the tethers. However, all of these nodes are spatially isolated from the core, supporting the single-mode assumption of the ridged waveguide in this design.

4.2.2 Static Filters

Measuring the filters' response follows the same procedure as per waveguides. However, in this case we are interested in the filter response shape, not the contrast ratio of oscillation. Ideally, the response should have a single, narrow, well-defined peak above a near-zero field. However, the response will have the same high-frequency oscillation present in the straight waveguides. As light travels serially through the resonators, these

61

oscillations are *multiplicative* with the desired response, requiring an enve-
lope to be taken of the measured response. (Alternatively, if the undesired
signal was known, it could be divided out.)

As the filter's response is strongly dependant upon physical dimen-
sions, it is unlikely any fabricated device will exactly match design and
simulation. In the case of a filter designed for 1550 nm, as little as a 50 nm
error in line width and the peak is pushed out of the scan range. To counter
this, designs with 25 nm offsets were added (as described in section 2.2).

To facilitate a quantitive analysis of the filter behavior, the raw mea-
surements were stripped of any oscillations from the waveguide by using
an envelope calculator listed in section B.3 of the appendix, and this data
was fit to a Lorentzian distribution using a non-linear least squares fit.
This fit included four terms: amplitude, center position, full-width half-
max, and constant offset. The first three are direct constituants of the dis-
tribution while the offset serves to account for the noise floor. Illustrated
in figure 4.5 is the measured optical response from a filter with a 1550 nm
long cavities (+25 nm correction factor) and a filter with a 725 nm long
cavity (no correction factor).

The shorter cavity has a line width of 13.7 nm at a center wavelength
of 1620 nm for a quality factor of 118. The longer cavity exhibited a line
width of 15.5 nm at a center wavelength of 1550 nm for a quality factor
of 100. Discussion of finesse is largely irrelevant as the free spectral range
exceeds both the range of the laser sweep and the high reflectivity band of
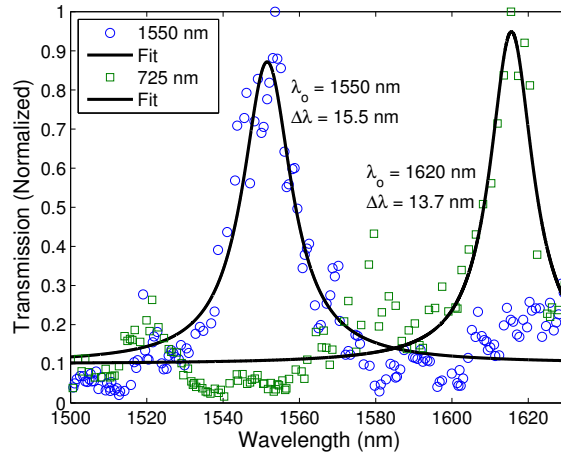
Figure 4.5: Measured response from static filters. A full-wavelength (1550 nm cavity) and a half-wavelength (725 nm cavity) filter were tested.

the mirrors. The decreased quality of the longer cavity can be attributed to multiple possible reasons: the longer cavity increasing losses to divergence, location of the peak in the mirror high-reflectivity band, differences in sidewall quality, or even variances in the quality of measured data for the fit. However, differences of 10% in linewidth are not significant.

Using this data, we can attempt to correlate measurements with the model for surface roughness. Performing a least squares fit of the model from section 2.3.2 to the full-wavelength data in figure 4.5 on variables of linewidth error, surface roughness, and linear scaling factor, we obtain the curve in figure 4.6. With a coefficient of determination (R^2) of 90%, the RMS surface roughness is calculated to be 29.4 nm, consistent with the visual estimate of 50 nm from [19]. Qualitative features of the curve reinforces the quality of the fit, namely the right-hand tail of the data cor-

63
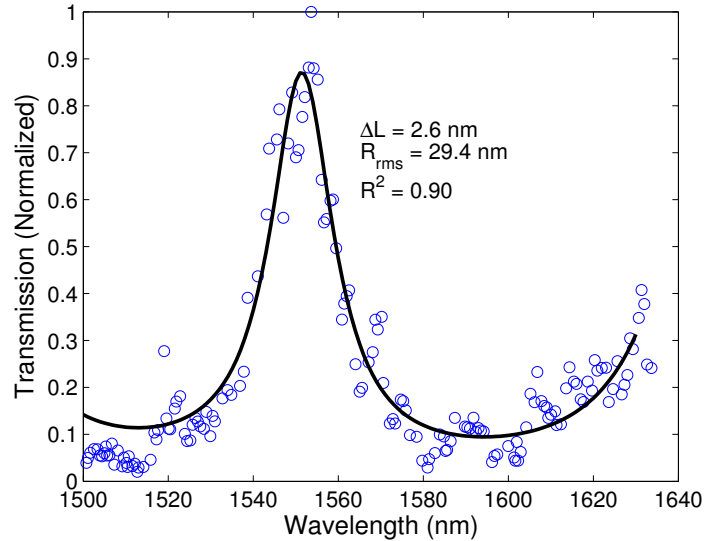
Figure 4.6: Fit of roughness model to measured data.

responds to the end of the high-reflectivity zone predicted by the model.

4.2.3 Tunable Filters

The tunable filter is a superset of the static filters. As described in section 2.2, a second, back cavity is introduced into the filter in order to suspend one of the Bragg mirrors, allowing the main cavity to be tuned. This introduces additional facets to scatter light as well an additional micron of unguided length for light to diverge. These effects are expected to result in an increase in line width. Furthermore, the mechanical suspension will introduce an additional point of failure for a device.

One device with a full-wavelength (1550 nm) cavity, -25 nm correction factor, and 500 μm suspension was found to be fully operational and

(a)   (b)
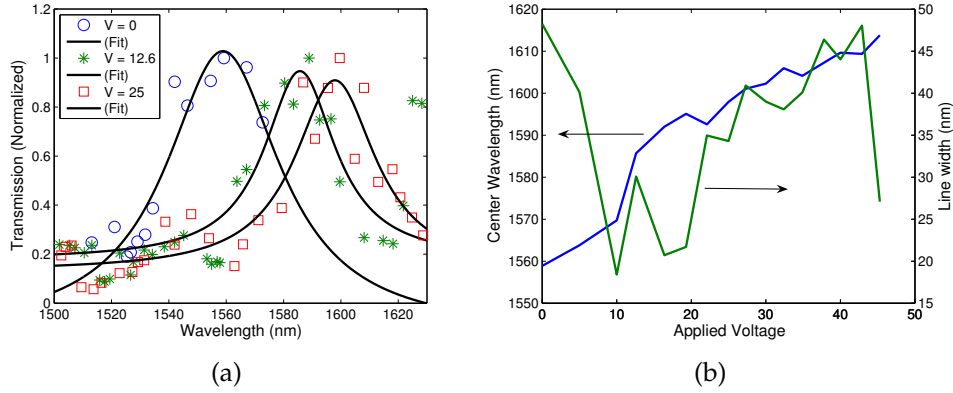
Figure 4.7: Measured response from tunable filter.

tested. The optical response is illustrated in figure 4.7(a) for the static condition in addition to applied potentials of 12.6 and 25 Volts. If we calculate the same lorentzian fit as performed for the static filters, we get the plot in figure 4.7(b), providing an average linewidth of 35.8 nm and an approximate Q of 45. The general trend towards increased linewidth as the filter tunes is expected: reflectivity of the Bragg mirror decreases as the wavelength shifts further from the $\lambda_o/4$ condition.

Continuing the analysis, fitting the response with no potential applied to the static model, we have a lithographic error of approximately 23 nm. According to the model introduced in section 2.3.3, we can expect the relationship between center wavelength and displacement shift in center wavelength is linear with slope of 0.40 nm center wavelength shift per nanometer of displacement. Comparing the measured center wavelength with the model, we generate the plot in figure 4.8. The experimental data
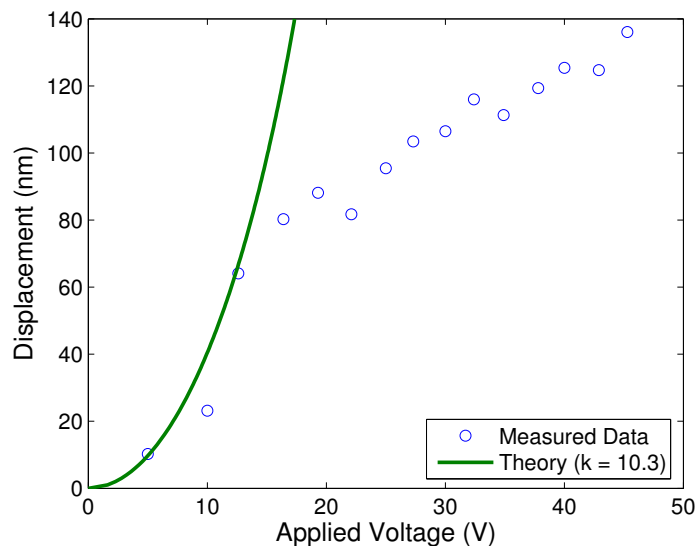
Figure 4.8: Beam displacement versus applied voltage.

confirms the model up to a displacement of approximately 80 nm, after which the data exhibits a linear rise while the model predicts a quadratic relationship. This is most likely due to the passband merging into the edge of the Bragg mirror stopband. But this demonstrates a possible tuning range of at least 40 nm in a single direction. Given the bidirectional tuning capabilities of the filter, this corresponds to a total 80 nm tuning range. This could not be tested as the device was tested to failure (stiction to the substrate) in a single direction.

4.3 Silicon Devices

Characterization of the Silicon devices was performed under the same equipment as for the Indium Phosphide devices; however, I was unsuccessful in coupling light through the waveguide. Concluding the doping of the device layer was too high, a set of high-resistance SOI wafers were purchased and the process, after further refinements, was repeated on these wafers. Again, I was unsuccessful in coupling optical power through the devices. At this time, the decision was made to abandon the silicon devices until the silicon process could be more thoroughly designed and characterized.

As illustrated in the analysis of the Indium Phosphide devices, surface roughness plays a considerable role in the performance of the devices. The goal of the silicon devices was to utilize a more sophisticated etching technique in order to reduce surface roughness. However, this introduced a wide variety of new fabrication techniques that did not undergo the same level and length of development as the Indium Phosphide techniques. Furthermore, the development process sought to reuse the mask set designed for Indium Phosphide. This lead to some problems, such as compromising the Aluminum contacts during sacrificial release, that were not successfully resolved.

If the underlying issue is optical loss, there are several techniques that can be applied to reduce it further: As silicon dioxide is not dissipative

(unlike the sacrificial layer in the indium phosphide system), future revisions of the silicon devices can dispense with the suspension. The exposed sidewall and aperiodic tethers act as a potential source of unnecessary loss. Further, work in silicon optical systems, such as in [2], have used alternating processes of thermal oxidation and HF etching to reduce surface roughness. However, this process would need to be carefully balanced with the buried oxide thickness or be performed prior to the final breakthrough.

Chapter 5

Conclusion

5.1 Summary of Results

Indium Phosphide ridged waveguides were constructed and exhibited loss on the order of 5.3 dB/cm to 9.2 dB/cm. Single mode operation was confirmed by rastering a lensed fiber across the exit facet of a waveguide.

Indium Phosphide tunable filters were successfully fabricated and test, exhibiting linewidths on the order of 15 nm (static filters). This is consistent with the predictions of numerical models for an RMS surface roughness of 30 nm, consistent with prior research in our fabrication technique. Numerical fits of experimental data to this model have R^2 values in excess of 90%. Tunable filters exhibited a wider linewidth, 35 nm. This is expected from the addition of a second cavity (necessary for movement) as well as the very act of tuning. The position of the peak wavelength is

consistent with numerical models up to a shift of approximately 40 nm, achieved at 15 Volts.

Silicon devices were fabricated but failed to function during testing. Multiple attempts to refine the process and use higher grades of wafers ultimately failed to produce a functional device. Success implementation will require future development of our SOI optical abilities.

5.2 Future Work

Future research into tunable filters will occur on multiple fronts: shrinking the device footprint, decreasing the linewidth, increasing or shifting the tuning range, and integrating with other photonic systems.

While the filter itself is small, approximately 17.6 μm long and 6 μm wide, the suspension and electrostatic actuator consume significantly greater space. In order to realize a cost-effective high-density integration, the device will need to be decreased in size further. Folded flextures could significantly decrease the linear length of the doubly-clamped suspension while decreasing the operating voltages further. However, such a design would also make the device more susceptible to stiction.

Decreasing the linewidth occurs along two paths: decreasing surface roughness to reduce scattering losses and decreasing the unguided cavity length to reduce losses to divergence. The first can be accomplished by moving from a cyclic RIE etch to an Inductively Coupled Plasma (ICP)

etcher: Etched samples from Oxford have exhibited sidewall roughness on the order of 2 nm, measured by Atomic Force Microscopy (AFM). Such low levels of roughness would reduce scattering losses below those expected from divergence. Divergence can be reduced by shorting the length of the unguided cavity. Assuming the required motion for tuning is a small fraction of the cavity length, the rest of the length can be folded into a waveguide, as was demonstrated in [8].

For spectrographic applications, the tuning range would need to be moved to more interesting bands, such as the Far-IR or visible light regions. While different materials would obviously be required for transmission, the 7/4th order Bragg mirrors would provide insufficient bandwidth. Improved designs would require 1/4th order Bragg mirrors, likely patterned with electron or ion beam. If even further bandwidth is required, the individual periods of the mirror could be of different length, broadening the bandwidth, but generating a more complex composite reflection coefficient in the process.

In the end, the device is only practical if it can be integrated with other photonic systems. In the communications space, this is simple, as detectors and emitters can be fabricated on chip. For the case of a traveling wave detector, this has been demonstrated in [23] with minimal modification to the existing layer structure. A tunable source could be constructed by placing a gain region within the filter cavity. Given the optically passive nature of the filter, it could share the same layer structure as more

sophisticated devices, such as modulators and optical amplifiers, so long as the layer structure can be biased to transparency and includes a sacrificial layer between the waveguide and substrate.

Appendix A

Transfer Matrices

In any design process, it is first necessary to develop a model to describe the operation of the intended product. Without such a model, it is impossible to establish the design parameters and tolerances without the expensive and time-consuming approach of trial and error.

A.1   Transmission Equations

Our filter, similar to the majority of shipping filters, is to be based on a one-dimensional photonic bandgap. This decision allows us to make use of the transmission equations, a system where a monochromatic wave traveling in the z-direction can be modeled with a simple analytical expression:

$$E(x,y,z,t) = E_0 u(x,y) exp(\omega t - ikz) \tag{A.1}$$

where k is the wavevector, $u(x,y)$ is the mode shape, ω is the angular frequency, t is time, and E_0 is the field amplitude.

For a plane wave, the mode shape in (A.1) is spatially-independent and k is calculated from the material's index of refraction. For a guided wave, $u(x,y)$ is a function of the waveguide's geometry and k has additional influences from this geometry. In both cases, the wavevector k can be calculated from the material or effective complex index of refraction $\tilde{n}$:

$$k = \frac{2\pi\tilde{n}}{\lambda_0} \tag{A.2}$$

The complex index of refraction $\tilde{n}$ is generally described to be composed of two parts: the real part providing the ratio of vacuum speed to to local speed, and an imaginary part quantifying loss due to conductivity, electrical excitation, and free-carrier absorption. Both of these parts contribute to the behavior at interfaces.

Using (A.1), it is possible to establish a relationship of the field strength and phase between any two points along the propagation vector in a homogeneous material:

$$E^+(z_1) = exp(ik(z_2 - z_1))E^+(z_2) \tag{A.3a}$$

$$E^-(z_1) = exp(-ik(z_2 - z_1))E^-(z_2) \tag{A.3b}$$

Or, in matrix notation:

$$
\begin{bmatrix} E^+ \\ E^- \end{bmatrix}_1 = \begin{pmatrix} exp(ik(z_2 - z_1)) & 0 \\ 0 & exp(-ik(z_2 - z_1)) \end{pmatrix} \begin{bmatrix} E^+ \\ E^- \end{bmatrix}_2 \tag{A.4}
$$

At an interface between two media, reflection, transmission, mode mismatch, and scattering will result in a redistribution of energy between the $+k$ and $-k$ waves. Ignoring complications from scattering and mode mismatch, the relationships are the Fresnel equations for normal incidence ($+k$ direction):

$$
r_{+k} = \frac{E_1^-}{E_1^+} = \frac{\tilde{n}_1 - \tilde{n}_2}{\tilde{n}_1 + \tilde{n}_2} \tag{A.5a}
$$

$$
t_{+k} = \frac{E_2^+}{E_1^+} = \frac{2\tilde{n}_1}{\tilde{n}_1 + \tilde{n}_2} \tag{A.5b}
$$

As with propagation, (A.5) is a linear operation and can also be represented as a matrix operation:

$$
\begin{bmatrix} E^+ \\ E^- \end{bmatrix}_{left} = \frac{1}{t_{+k}} \begin{pmatrix} 1 & r_{+k} \\ r_{+k} & 1 \end{pmatrix} \begin{bmatrix} E^+ \\ E^- \end{bmatrix}_{right} \tag{A.6}
$$

By performing the substitutions and replacing $\tilde{n}$ with k, we obtain the final form:

$$
\begin{bmatrix} E^+ \\ E^- \end{bmatrix}_{left} = \begin{pmatrix} \frac{k_1 + k_2}{2k_1} & \frac{k_1 - k_2}{2k_1} \\ \frac{k_1 - k_2}{2k_1} & \frac{k_1 + k_2}{2k_1} \end{pmatrix} \begin{bmatrix} E^+ \\ E^- \end{bmatrix}_{right} \tag{A.7}
$$

The beauty in (A.4) and (A.7) is that given a complicated stack of dielectric layers, one need only chain the two matrices to find the behavior of the system. Beginning with the identity matrix, one need only multiply by the matrix in (A.7) each time the index changes and by the matrix in (A.4) when traveling through a material. Non-homogeneous materials can be approximated by using short spans of homogeneous material with small steps in index.

A.2   Wavelength Dependent Index

For all materials, the index of refraction is a function of the wavelength. In fact, the real and imaginary terms of the index of refraction are related by the Kramers-Kronig relationship:

$$Re\{\tilde{n}(E)\} = n(\infty) + \frac{2}{\pi} \cdot \mathcal{P} \int_0^\infty \frac{Im\{\tilde{n}(E')\}}{E'^2 - E^2} dE' \qquad (A.8)$$

Where E is the photon energy, $n(\infty)$ is the index at DC, and $\mathcal{P}$ denotes the Cauchy principal value.

One common model fitting the requirement of (A.8) is derived from the concept of anharmonic oscillators:

$$\tilde{n}^2 = n(\infty) + \sum_n \frac{A_n}{E^2 - E_n^2 + i\Gamma_n E} \qquad (A.9)$$

A.3   Waveguides and Coupling Efficiency

The mathematics described in A.1 can also be applied to guided optics containing a single mode. In this case, the effective index of the mode is used instead of the physical index of the material. However, an additional complication arises at interfaces: modal mismatch between the two waveguides.

The fraction of coupling between two modes is calculated by the overlap integral of their fields [24]:

$$a = \frac{\iint s(x,y)u(x,y)dxdy}{\sqrt{\iint |s(x,y)|^2dxdy \iint |u(x,y)|^2dxdy}} \tag{A.10}$$

where s is the field distribution of the incident wave and u is the field distribution of the transmitted wave. It should be noted that when s is the same as u, a is 1 as is the case for reflected waves.

The interface matrix derived in (A.7) can be revised to include the coefficient calculated in (A.10):

$$\begin{bmatrix} E^+ \\ E^- \end{bmatrix}_{left} = \begin{pmatrix} \frac{1}{t} & \frac{r}{t} \\ \frac{r}{at} & \frac{r^2}{at} + \frac{atn_2}{n_1} \end{pmatrix} \begin{bmatrix} E^+ \\ E^- \end{bmatrix}_{right} \tag{A.11}$$
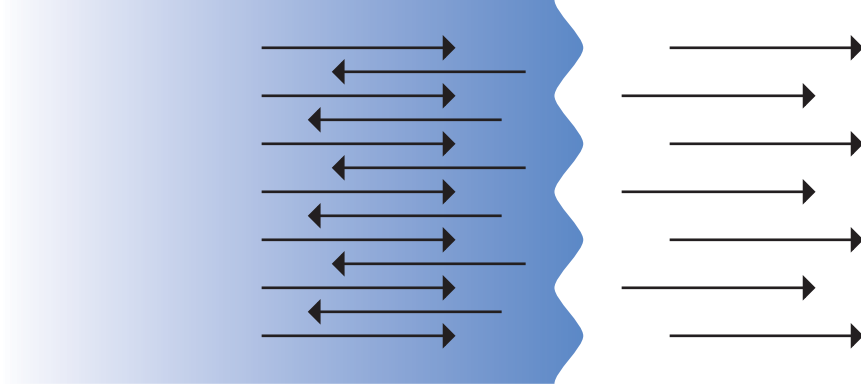
Figure A.1: Schematic of Huygen's diffraction at material interface.

expanding r and t as before:

$$
\begin{bmatrix} E^+ \\ E^- \end{bmatrix}_{left} = \begin{pmatrix} \frac{k_1+k_2}{2k_1} & \frac{k_1-k_2}{2k_1} \\ \frac{k_1-k_2}{2ak_1} & \frac{(k_1-k_2)^2+4a^2k_1k_2}{2ak_1(k_1+k_2)} \end{pmatrix} \begin{bmatrix} E^+ \\ E^- \end{bmatrix}_{right}
\tag{A.12}
$$

A.4   Interface roughness

A reality of all systems is that the interfaces between two mediums will not be perfectly smooth. For guided optics, this is especially problematic as the various etch processes used to form facets and etalons leave roughness significantly greater than those produced by epitaxial growth or cleavage.

The most straightforward model for modeling surface roughness is to begin with Huygen's diffraction. As illustrated in figure A.1, the surface of the interface is modeled as a continuum of points. Any displacement in the interface from the mean will result in a phase shift at that point:

$$\Delta\phi_{transmit} = \Delta d \cdot \left[k_{left} - k_{right}\right]$$

$$\Delta\phi_{reflect} = 2 \cdot \Delta d \cdot k_{left}$$

where Δd is the displacement due to roughness, k_{left} is the wavevector of the incident wave, and k_{right} is the wavevector of the transmitted wave. It is normally assumed surface roughness has a Gaussian distribution:

$$p\left(\triangle d\right) = \frac{1}{\sigma\sqrt{2\pi}} \exp\left(-\frac{\triangle d^2}{2\sigma^2}\right)$$

Integrating phase over the distribution leads to scaling factors for both reflection and transmission:

$$r' = r \int\limits_{-\infty}^{+\infty} \frac{1}{\Delta\phi\sqrt{2\pi}} e^{-\phi^2/2\Delta\phi^2} e^{i\phi} d\phi = r \cdot e^{-\left(2\cdot\Delta d\cdot k_{left}\right)^2/2}$$

$$t' = t \int\limits_{-\infty}^{+\infty} \frac{1}{\Delta\phi\sqrt{2\pi}} e^{-\phi^2/2\Delta\phi^2} e^{i\phi} d\phi = r \cdot e^{-\left(\Delta d\cdot\left[k_{left}-k_{right}\right]\right)^2/2}$$

The new reflection and transmissions coefficients can be substituted for the original values calculated from the index of the refraction.

A.5 Divergence

One of the concerns in a guided optics project are the loses that result as light leaves one guided region and propagates through air. To determine these loses, it is typical to approximate the wave in the unguided region as a Gaussian beam:

$$E(r,z) = E_o \frac{w_o}{w(z)} \exp\left(\frac{-r^2}{w^2(z)}\right) \exp\left(-ikz - ik\frac{r^2}{2R(z)} + i\zeta(z)\right) \quad \text{(A.13)}$$

z is the distance from the origin (beam waist) along the direction of propagation. r is the distance from the beam center (z axis). w_0 is the beam radius at the beam waist. $w(z)$, $R(z)$, and $\zeta(z)$ are functions of position defined as:

$$w(z) = w_0\sqrt{1 + \left(\frac{z}{z_o}\right)^2} \quad \text{(A.14a)}$$

$$R(z) = z\left[1 + \left(\frac{z_o}{z}\right)^2\right] \quad \text{(A.14b)}$$

$$\zeta(z) = tan^{-1}\left(\frac{z}{z_o}\right) \quad \text{(A.14c)}$$

Where z_o is the Rayleigh range, the primary parameter controlling beam expansion:

$$z_o = \frac{\pi w_o^2}{\lambda}$$

The goal is to determine the coupling from the expanded beam to the receiving waveguide. If we assume the initial mode shape is equivalent to
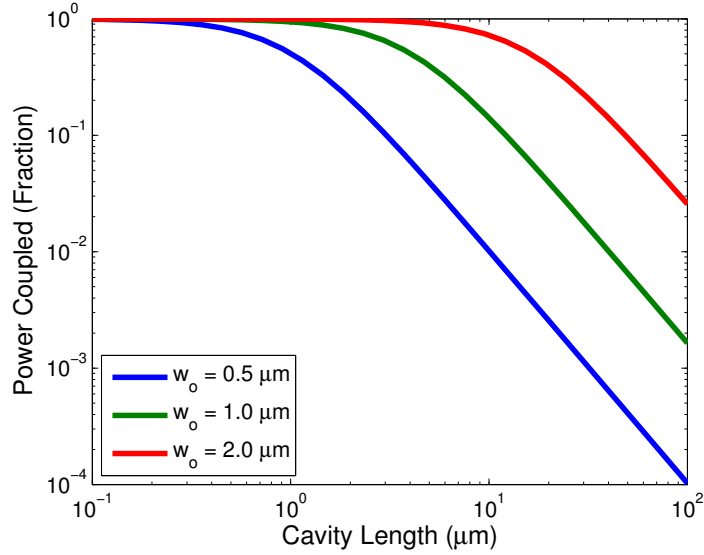
Figure A.2: Coupled power versus cavity length for a 1550 nm wavelength Gaussian beam.

the mode shape of the receiving waveguide, we can simply perform the overlap integral described in section A.3:

$$a = \frac{2\pi w_o^2 \left(\pi w_o^2 + i\, z\lambda\right)}{\left(2\pi^2 w_o^4 + z^2\lambda^2 + i\,\pi w_o^2 z\lambda\right)} \exp\left(-i\,kz\right)$$

If we evaluate the above expression for a wavelength of 1550 nm and multiple beam lengths, we get the plot of coupled power versus cavity length illustrated in figure A.2. Clear from the plot is that for cavity lengths (z) far less than the beam waist, power loss is minimal; however, once the cavity length exceeds the beam waist, loss increases significantly. Therefore, the waveguide must have a mode diameter of similar magnitude to any cavity lengths or risk losing significant power.

It is important to emphasize that the use of the Gaussian beam is an approximation. Real waveguides, especially asymmetrical ones like ridged waveguides, will have more complex mode shapes that diverge more rapidly than the Gaussian beam. A more accurate method would be to calculate the mode cross-section (as was performed in section 2.3.1 using Finite Element), take the two-dimensional Fourier transform, and compute the phase shift of the individual components. However, the marginal increase in accuracy of this method is largely unnecessary and it does not provide an analytical design expression.

Appendix B

Programs

B.1 Static Filter Model

```
function T = FilterNoBack(n, lambda, A, lineerror)
%FILTERNOBACK Simulates propagation through a static filter
%  FILTERNOBACK(N, LAMBDA, A, ERROR) is the transmission coefficient (T)
%  of wavelengths LAMBDA (meters) through a Fabry-Perot filter with RMS
%  facet roughness A (meters) and lithography linewidth error ERROR
%  (meters).
error(nargchk(2, 4, nargin, 'struct'));
if(nargin < 3),
    A = 0;
end
if(length(lambda) > 1),
    T = zeros(size(lambda));
    for k=1:numel(lambda),
        T(k) = FilterNoBack(n, lambda(k), A, lineerror);
    end
    return;
end

% Calculate wavevectors
k = 2*pi*n/lambda;
k0 = 2*pi/lambda;
% Calculate roughness/coupling terms
pt = exp(-0.5 * (A * (k - k0))^2);
pra = exp(-0.5 * (2 * A * k0)^2);
pri = exp(-0.5 * (2 * A * k)^2);
% Calc interface matrices
Iai = [ (k0+k)/(2*pt*k0) (k0-k)*pra/(2*k0*pt) ;
```

```
        (k0-k)*pra/(2*k0*pt)  (pra*(k0-k)^2+4*k0*k*pt^2)/(2*(k0+k)*k0*pt) ];
Iia = [ (k+k0)/(2*pt*k)  (k-k0)*pri/(2*k*pt) ;
        (k-k0)*pri/(2*k*pt)  (pri*(k-k0)^2+4*k0*k*pt^2)/(2*(k+k0)*k*pt) ];
% Dimensions
Lgap = 1.55E-6-lineerror;      % Length of Gap
Lslab = 0.849E-6+lineerror;    % Width of InP Slab
Lair = 1.163E-6-lineerror;     % Width of Air Slab
Pgap = [exp(i*k0*Lgap) 0; 0 exp(-i*k0*Lgap)];
Pslab = [exp(i*k*Lslab) 0; 0 exp(-i*k*Lslab)];
Pair = [exp(i*k0*Lair) 0; 0 exp(-i*k0*Lair)];
% Generate Matrices
Tmirror = Pair * Iai * Pslab * Iia * Pair * Iai ...
    * Pslab * Iia * Pair * Iai * Pslab;
T = Iia * Tmirror * Iia * Pgap * Iai * Pslab ...
    * Iia * Tmirror;
T = abs(1 / T(1,1)^2);
```

B.2   Waveguide Loss Calculator

```
function [waveout, loss] = calcloss(wavelength, transmit)
% CALCLOSS    Calculates the wavelength-dependant waveguide loss
%    [ lambda, loss ] = CALCLOSS(lambda, transmit) calculates the waveguide
%    loss as a function of wavelength by approximating the solution to the
%    Airy function.  The spectrum is divided into 0.5 nm sections and the
%    minimum and maximum are determined.  The contrast ratio is then used to
%    determine loss.

% Theoretical reflectivity
%    n=3.195 for Indium Phosphide
%    n=3.45  for Silicon
R = ((3.45 - 1) / (3.45 + 1)) ^ 2;

% Length of transmission band (nm)
dL = 0.5;
% Number of datapoints per band
n = ceil(dL / (wavelength(2) - wavelength(1)));

% Run through bands
K = [];
waveout = [];
for i = 1:n:length(wavelength),
    if(i + n - 1 > length(wavelength)),
        break
    end
    % Find max and min in band
    [max_T, max_I] = max(transmit(i:i+n-1));
    [min_T, min_I] = min(transmit(i:i+n-1));
    % Calculate contrast and wavelength
    K = [ K (max_T-min_T)/(max_T+min_T) ];
    waveout = [ waveout 0.5*(wavelength(min_I+i)+wavelength(max_I+i))];
end

% Convert into loss
```

```
Rloc = (1 - sqrt(1 - K .^ 2)) ./ K;
loss = 10*log10(R ./ Rloc);
```

B.3   Envelope Calculator

```
function [xf, yf] = envelope(xi, yi, n)
%ENVELOPE    Calculates the envelope of a function
%   [x, y] = ENVELOPE(x, y) is the envelope of signal (x, y), calculated
%   by finding those points preceeded by two points of lower y and followed
%   by points equal-or-less-than y.  This descrepancy is to ensure mesas
%   are properly detected while being returned only once (at the leading
%   edge).
%
%   [x, y] = ENVELOPE(x, y, n) repeats the envelope function n times.
if(nargin < 3),
    n = 1;
end

for j = 1:n,
    xf = [];
    yf = [];
    for i = 3:length(xi)-2,
        % We are at a peak if the preceeding two points are less and the next
        % two are less than or equal (in case we have a mesa)
        if((yi(i - 2) < yi(i)) && (yi(i - 1) < yi(i)) ...
                && (yi(i + 1) <= yi(i)) && (yi(i+2) <= yi(i))),
            xf = [ xf xi(i) ];
            yf = [ yf yi(i) ];
        end
    end
    xi = xf;
    yi = yf;
end
```

85

Bibliography

[1] D. Hohlfeld, M. Epmeier, and H. Zappe, "A thermally tunable, silicon-based optical filter," *Sensors and Actuators A: Physical*, vol. 103, pp. 93–99, 2003.

[2] S.-S. Yun and J.-H. Lee, "A micromachined in-plane tunable optical filter using the thermo-optic effect of crystalline silicon," *Journal of Micromechanics and Microengineering*, vol. 13, no. 5, pp. 721–725, Sep. 2003.

[3] D. Hohlfeld and H. Zappe, "Thermally tunable optical thin-film filters with sub-nanometer resolution and 41.7 nm continuous tuning range," in *18th IEEE International Conference on Micro Electro Mechanical Systems*. IEEE, 2005, pp. 100–103.

[4] H. Gan, H. Zhang, C. T. DeRose, R. A. Norwood, N. Peyghambarian, M. Fallahi, J. Luo, B. Chen, and A. K.-Y. Jen, "Low drive voltage Fabry-Perot etalon device tunable filters using poled hybrid sol-gel

materials," *Applied Physics Letters*, vol. 89, no. 4, pp. 41 127–1–3, July 2006.

[5] C. A. Barrios, V. R. de Almeida, and M. Lipson, "Low-power-consumption short-length and high-modulation-depth silicon electrooptic modulator," *IEEE/OSA Journal of Lightwave Technology*, vol. 21, no. 4, pp. 1089–1098, Apr. 2003.

[6] C. A. Barrios, V. R. Almeidaand, R. R. Panepucci, B. S. Schmidt, and M. Lipson, "Compact silicon tunable Fabry-Perot resonator with low power consumption," *IEEE/OSA Journal of Lightwave Technology*, vol. 16, no. 2, pp. 506– 508, Feb. 2004.

[7] C. Seassal, J. L. Leclercq, X. Letartre, A. Gagnaire, M. Gendry, P. Viktorovitch, J. P. Laine, F. Sidoroff, R. Ledantec, T. Benyattou, and G. Guillot, "Micromachined structures for vertical microelectrooptical devices on InP," in *Indium Phosphide and Related Materials, 1996. IPRM '96., Eighth International Conference on*, Schwabisch-Gmund, Germany, Apr. 1996, pp. 275–278.

[8] M. Garrigues, J. Danglot, J.-L. Leclercq, and O. Parrillaud, "Tunable high-finesse InP/air MOEMS filter," *IEEE Photonics Technology Letters*, vol. 17, no. 7, pp. 1471–1473, Jul. 2005.

[9] M. W. Pruessner, T. King, D. Kelly, R. Grover, L. Calhoun, and R. Ghodssi, "Mechanical property measurement of InP–based MEMS for

optical communications," *Sensors and Actuators A: Physical*, vol. 105, no. 2, pp. 190–200, 2003.

[10] M. W. Pruessner, K. Amarnath, M. Datta, D. Kelly, S. Kanakaraju, P. T. Ho, and R. Ghodssi, "InP-based optical waveguide MEMS switches with evanescent coupling mechanism," *IEEE/ASME Journal of Micro-electromechanical Systems*, vol. 14, no. 5, pp. 1070–1081, Oct. 2005.

[11] A. Lipson and E. M. Yeatman, "A 1-d photonic band gap tunable optical filter in (110) silicon," *IEEE/ASME Journal of Microelectromechanical Systems*, vol. 16, no. 3, pp. 521–527, Jun. 2007.

[12] C. Li and A. W. Poon, "Active silicon microring resonators using metal-oxide-semiconductor capacitors," in *1st IEEE International Conference on Group IV Photonics*, 2004, pp. 19–21.

[13] U. Levy, K. Campbell, A. Groisman, S. Mookherjea, and Y. Fainman, "On-chip microfluidic tuning of an optical microring resonator," *Applied Physics Letters*, vol. 88, p. 111107, 2006.

[14] D. Kelly, M. W. Pruessner, K. Amarnath, M. Datta, S. Kanakaraju, L. C. Calhoun, and R. Ghodssi, "Monolithic suspended optical waveguides for InP MEMS," *IEEE Photonics Technology Letters*, vol. 16, no. 5, pp. 1298–1300, 2004. [Online]. Available: http://ieeexplore.ieee.org/xpls/abs_all.jsp?arnumber=1291490

[15] J. R. D. Whaley, M. H. Kwakernaak, V. B. Khalfin, S. A. Lipp, W. K. Chan, H. An, and J. H. Abeles, "Observation of low optical overlap mode propagation in nanoscale indium phosphide membrane waveguides," *Applied Physics Letters*, vol. 90, pp. 011 114–1–3, January 2007. [Online]. Available: http://scitation.aip.org/getabs/servlet/GetabsServlet?prog=normal&id=APPLAB000090000001011114000001&idtype=cvips&gifs=yes

[16] K. K. Lee, D. R. Lim, H.-C. Luan, A. Agarwal, J. Foresi, and L. C. Kimerling, "Effect of size and roughness on light transmission in a si/SiO_2 waveguide: Experiments and model," *Applied Physics Letters*, vol. 77, no. 11, pp. 1617–1619, September 2000. [Online]. Available: http://scitation.aip.org/getabs/servlet/GetabsServlet?prog=normal&id=APPLAB000077000011001617000001&idtype=cvips&gifs=yes

[17] R. Soref, J. Schmidtchen, and K. Petermann, "Large single-mode rib waveguides in GeSi-Si and Si-on-SiO$_2$," *IEEE Journal of Quantum Electronics*, vol. 27, no. 8, pp. 1971–1974, Aug. 1991.

[18] S. Pogossian, L. Vescan, and A. Vonsovici, "The single-mode condition for semiconductor rib waveguides with large cross section," *IEEE/OSA Journal of Lightwave Technology*, vol. 16, no. 10, pp. 1851–1853, Oct. 1998.

[19] M. W. Pruessner, N. Siwak, K. Amarnath, S. Kanakaraju, W. H. Chuang, and R. Ghodssi, "End-coupled optical waveguide MEMS devices in the indium phosphide material system," *Journal of Micromechanics and Microengineering*, vol. 16, pp. 832–842, Apr. 2006.

[20] R. Grover, J. V. Hryniewicz, O. S. King, and V. Van, "Process development of methane–hydrogen–argon-based deep dry etching of InP for high aspect-ratio structures with vertical facet-quality sidewalls," *Journal of Vacuum Science and Technology B*, vol. 19, no. 5, pp. 1694–1698, September 2001. [Online]. Available: http:// scitation.aip.org/getabs/servlet/GetabsServlet?prog=normal&id= JVTBD9000019000005001694000001&idtype=cvips&gifs=yes

[21] D. J. Thomas, K. Powell, M. M. Bourke, Y. P. Song, and C. Fragos, "High density plasma etch processes for the manufacture of optoelectronic devices based on InP," in *International Conference on Compound Semiconductor Manufacturing Technology*, 2001, p. 9B_3.

[22] R. Regener and W. Sohler, "Loss in low-finesse Ti:LiNbO$_3$ optical waveguide resonators," *Applied Physics B: Lasers and Optics*, vol. 36, no. 3, pp. 143–147, Mar. 1985.

[23] N. P. Siwak, "Indium phosphide mems cantilever waveguides for chemical sensing with integrated optical readout," Master's thesis, University of Maryland, College Park, MD, Oct. 2007.

[24] B. E. A. Saleh and M. C. Teich, *Fundamentals of Photonics*.   New York, NY: Wiley Interscience, 1991, pp. 261–262.